Theoretical and experimental mechanical properties and thermal conductivity of W-Al-B thin films deposited by magnetron sputtering

Ewa Wojtiuk [a,*] , Marcin Maździarz [a], Tomasz Stasiak [b], Marcin Brykała [b],
Marcin Chmielewski [b,c], Mateusz Włoczewski [a,d], Anna Kosińska [e], Katarzyna Zielińska [a],
Oksana Haponova [a,f], Jarosław Jasiński [b,e], Tomasz Mościcki [a,*]

[a] Institute of Fundamental Technological Research, Polish Academy of Sciences, Pawinskiego 5B, Warsaw 02-106, Poland
[b] Materials Research Laboratory, National Centre for Nuclear Research, A. Soltana 7, Otwock 05-400, Poland
[c] Łukasiewicz Research Network – Institute of Microelectronics and Photonics, Centre of Functional Materials, Wolczynska 133, Warsaw 01-919, Poland
[d] Faculty of Materials Science and Engineering, Warsaw University of Technology, Wołoska 141, Warsaw 02-507, Poland
[e] NOMATEN Centre of Excellence, National Centre for Nuclear Research, A. Soltana 7, Otwock 05-400, Poland
[f] Applied Material Science and Technology of Constructional Materials Department, Sumy State University, Kharkivska 116, Sumy 40007, Ukraine

ARTICLE INFO

ABSTRACT

This work compares experimentally measue properties of W-Al-B thin films with mechanical properties, density, and thermal conductivity values calculated using DFT methods. Theoretical modelling was conducted to simulate two WB_2 stable structures alloyed with varying amounts of aluminium: α-WB_2 (P6/mmm) and ω-WB_2 (P6$_3$/mmc), as well as α-AlB_2 (P6/mmm). Using the HiPIMS-DC magnetron sputtering technique, films with α-WB_2 structure and varying aluminium contents were deposited at 400 °C. When layers are composed with x = 1.4 % aluminium (where x = atAl / (atAl + at%W)), their microstructure changes from amorphous to crystalline columnar. A back transformation to an amorphous microstructure occurs when the amount of aluminium exceeds x = 7.3 %. An original method was used for the film density studies, which combined mass measurements and microscopic observation. These measurements were then used to determine the layers' thermal conductivity using the thermoreflectance method. The measured conductivity of the deposited ceramic films range from 3 to 6 W/(mK). Moreover, the obtained films are very hard, e.g. H = 36.1 ± 1.7 GPa for x = 1.4 % Al, but exhibit a much lower Young's modulus than the theoretical values. The relatively high H/E* ratio > 0.1 for films with low aluminium content indicates anmore elastic character. Ab-initio calculations showed that, based on the criteria of Cauchy pressure (C_{12}-C_{44}) and Pugh's ratio (B/G), the α-WB_2 structure may have a ductile nature in contrast to the other structures. However, the deposited films are rather brittle in nature, resulting from an excess of boron. The fracture toughness measurements show higher K_{IC} values for low aluminium content. They are 3.8 MPa$\sqrt{m}$ for WB_2, 2.8 MPa$\sqrt{m}$ for x = 1.4 %, and 3 MPa$\sqrt{m}$ for x = 7.3 % aluminium.

1. Introduction

Tungsten borides are attractive materials due to their exceptional properties, including hardness, thermal stability, chemical inertness, and electrical conductivity. These characteristics make them suitable for various applications, including wear-resistant coatings for tools and structural components in high-performance engine parts [1,2]. Despite progress in research on these materials, further theoretical and experimental work is necessary to enable their industrial implementation. The main challenges associated with borides are their brittleness and low oxidation resistance at high temperatures. In the case of oxidation, recent studies show that the use of alloying additives that are strong oxide formers, such as Al [3] or Si [4], significantly improves this property. However, understanding the phenomena behind these superior mechanical properties and explaining the cause of cracking requires theoretical studies at the atomic scale, combined with advanced experimental methods [5,6]. Although DFT studies have suggested phase transformations in TMB2s, calculations based on molecular dynamics (MD) simulations at finite temperature are uncommon due to the absence of reliable force fields or their limitations in achieving

---

quantum-level accuracy. Thus, in the latest research by Lin et al. [6], phase changes of TMB2s ($\alpha \to \omega$ transformation in WB_2) subjected to shear deformation were revealed by utilizing machine-learning potential molecular dynamics (ML-MD). Additionally, machine-learning interatomic potentials (MLIPs) were implemented to provide a comprehensive understanding of the initiation of fractures in transition metal borides and to accurately assess their fracture properties [7].

Alloyed tungsten diboride films exhibit improved toughness and resistance to cracking compared to their binary counterparts [8,9]. The most stable structure of WB_2 is P6$_3$/mmc polymorph. WB_2 like MoB_2 favours this structure because Mo and W are much more electronegative than other metals in groups IVB-VIB of the periodic table of elements, which leads to a significantly reduced charge transfer from TM to boride planes. This charge transfer is required to form planar graphite rings, for which the B atoms lack one electron. It is well known that tungsten diboride can also crystallize in a metastable P6/mmm phase with a AlB_2 like hexagonal structure [10]. However, vacancy stabilization is necessary [11]. A method that can introduce such defects is physical vapor deposition PVD, and in particular magnetron sputtering. Both mentioned polymorphs also differ in mechanical properties. Theoretical calculation shows ω-WB_2 P6$_3$/mmc is very hard $H = 34.3$ GPa with Young's modulus $E = 578$ GPa, while α-WB_2 P6/mmm is also hard, but its hardness is much lower ($H = 21.2$ GPa) with $E = 447$ GPa [12,13]. Therefore, alloying with aluminium or transition metals TM such as Ta, Ti, Zr can increase the hardness of this material, while maintaining a relatively high Young's modulus [8,12]. The increase in hardness can be attributed to solid solution hardening. This strengthening effect depends on the size difference between the solute and solvent atoms, the solute of the concentration, and the nature of the lattice distortion. A larger difference between the atomic radii of the solute and solvent atoms leads to greater lattice distortion and a stronger hardening effect. Pangilinan et al. [14] showed that alloying WB_2 with other elements with different atomic-size and valence electron quantity, such as tantalum or niobium, either substituing tungsten atoms or fitting into the spaces between them, strengthens the compound through solid-solution hardening. These foreign atoms cause local distortions in the lattice, which hinder the movement of dislocations. As a result, plastic deformation is more difficult, which increases the alloy's strength. The distortions around solute atoms interact with the stress fields of dislocations, creating an energy barrier that must be overcome for the dislocation to pass. This indicates that more shear stress is needed to maintain the plastic deformation. Because of this, the alloy gets stronger, and its yield strength goes up compared to the undoped WB_2.

The deposition of very hard thin films using magnetron sputtering is a significant research area in materials engineering. The synthesis of thin films through magnetron sputtering benefits from the ability to control their microstructural properties and ensure uniformity, which is crucial for enhanced mechanical and thermal performance. The utilization of magnetron sputtering, particularly the high-power impulse magnetron sputtering (HiPIMS) technique, has garnered significant attention recently for the deposition of thin films with tunable properties. This approach ensures high-quality film deposition, enabling researchers to manipulate various parameters and tailor material properties for specific applications. HiPIMS offers a distinct advantage over conventional sputtering techniques due to the high ionization potential of the sputtered material during deposition. This results in an enhancement of the ion-to-neutral ratio in the plasma, leading to improved film density and adhesion. In addition, the hybrid W_2B_5-HiPIMS/TMB$_2$-DCMS method (where DCMS - direct current magnetron sputtering) with synchronized bias enables the use of W-ion irradiation during film growth, resulting in increased density and hardness without the need for external substrate heating [3,15]. Recent studies have also shown that transition metal diboride (TMB$_2$) films alloyed with aluminium deposited using magnetron sputtering demonstrate improved oxidation resistance and hardness [16,17]. Moreover, the incorporation of aluminium into the boride structure has been shown to enhance the thermal stability and

mechanical properties of the films at elevated temperatures and under stress conditions [18]. Aluminium doping tends to increase the thermal stability of borides by promoting the formation of protective oxide (Al_2O_3) scale, which is crucial in high-temperature applications. The oxidation behaviour of aluminium boride films reveals the formation of protective oxide phases, enhancing their durability and resistance to degradation [18]. In addition, phase stability in aluminium borides is influenced by stoichiometry, where optimal ratios of aluminium to boron can lead to improved structural integrity [19]. When examining the mechanical properties of transition metal boride films alloyed with Al, a notable increase in hardness is observed compared to their undoped counterparts. For example, the hardness of Ti-Al-B films increases with aluminium content, reaching values exceeding 40 GPa in specific configurations [3,16].

Magnetron sputtering enables co-sputtering of multiple materials, thereby facilitating the production of layered structures that exhibit superior mechanical and functional properties. Research indicates that interactions among different sputtered species during deposition influences the microstructure and resultant properties of the films. For example, in the TiB$_2$ system, a combination of Ti and Al within a boride matrix has been found to yield films with higher thermal and mechanical stability [3]. One of the advantages of using magnetron sputtering for W-Al-B films is the precise control over the deposition parameters that influence the final film properties. It has been noted that increasing the sputtering power can enhance the deposition rate and improve the adhesion strength of thin films by increasing the energy of the bombarding particles [20]. Specifically, the ionized fraction of the sputtered material particles flux plays a crucial role here. It has been observed that under appropriate conditions, the growth of thin films is primarily governed by the ionized species rather than neutral ones, suggesting that the ionization potentials of W, Al, and B significantly influence deposition rates and film characteristics [3]. The preferential ejection of boron along the target normal, combined with the sputtering of aluminium and tungsten at differing angles, indicates that the relative positions of the elements in the deposited films may lead to either stoichiometric or non-stoichiometric compositions, which are often reflected in the mechanical properties of the thin films [21]. Moreover, the structural evolution during the deposition of doped tungsten boride coatings has been demonstrated to enhance hardness and wear resistance [22]. The presence of boron can also facilitate the formation of borides, which are noted for their exceptional hardness and thermal stability, attributes that are particularly beneficial in cutting and wear-resistant applications [23,24]. Moreover, the combination of doping aluminium with tungsten and boron can enhance the thermodynamic stability of the coatings, thereby improving their reliability in high-temperature applications [18,25]. However, it should be noted that to obtain crystalline W-Al-B films, DC magnetron sputtering requires heating the substrate to 700 ℃ or higher [18]. Such a high deposition temperature is necessary because deposition at around 500 ℃ results in an amorphous structure, and above 600 ℃ forms a small fraction of the α-AlB_2 crystalline phase [19].

The literature on boride thin films, primarily based on TEM observations, states that the deposited layers have a dense, defect-free structure. However, there is no information about the real density of such coatings [26]. This parameter, on the other hand, is important and must be incorporated into layer properties calculations at scales above the atomistic. Additionally, during experimental measurments of thin films thermal conductivity, e.g. using the nanosecond thermoreflectance technique, the density value is either needed [27]. As described earlier, ternary tungsten boride layers exhibit many interesting properties, and their fundamental physicochemical parameters are well understood, however to date, there are no experimental results on their thermal conductivity. The problem is interesting because the available thermal conductivity values for solid materials such as AlB_2 ($\kappa = 52$–66 W/mK [28]) or W_2B_5 ($\kappa = 47$ W/mK [29]) – similar in crystallographic structure to WB_2 significantly differ from the calculated theoretical values (WB_2 $\kappa = 2.017$ W/mK [30]). Moreover, no data are available on the

thermal properties of multiphase systems such as WB_2-AlB_2.

A thorough comprehension of the fundamental physical concepts and the unique characteristics of the materials involved at the atomistic scale is necessary for the theoretical modeling of tungsten boride coatings at the nano- and microscales. Currently, Density Functional Theory (DFT) studies of tungsten borides with different alloying elements only look at the α phase's elastic constants and phase stabilities, not competing structures like the γ or ω phases [31]. According to ab initio calculations, the stability of W-boride compounds with varying stoichiometries is particularly influenced by vacancies [32]. Moreover, theoretical investigations have demonstrated that the properties of novel compounds can be influenced by varying boron content [33] and by intentional alloying with elements such as aluminum or transition metals [11]. So far, theoretical calculations of the fracture resistance and thermal conductivity of such materials in the form of thin films remain limited. In the context of W-Al-B thin films, density functional theory (DFT) calculations provide essential insights into their structural stability and phase composition. Recent studies have highlighted the significance of DFT in predicting the formation of $W_{1-x}Al_xB_2$ solid solutions and assessing their stability in terms of stoichiometry and vacancy concentrations on their sublattices [18,25]. The theoretical results obtained so far for W-Al-B compounds have been related to the doping of the metastable P6/mmm structure. However, there are no such results for the more stable ω-WB_2 P6$_3$/mmc structure, which is present in bulk materials.

Considering the latest research on coatings from this group of materials [18,19], thin films of tungsten borides alloyed with aluminum have very high application potential. However, further research is needed to optimize the deposition rate and temperature to achieve the desired properties. In this article tungsten - aluminium - boron coatings will be deposited using a combined HiPIMS + DCMS magnetron method. The influence of high energy pulses on deposition rate and the temperature required to obtain crystalline coatings will be analyzed. Additionally, the influence of the aluminium content (0–100 % relative to tungsten) on the structure evolution and mechanical properties of the deposited films will be studied.

It is also necessary to develop a database of material properties that will enable theoretical analysis of the aforementioned layers under various types of loading and numerical simulations of the phenomena leading to their destruction. The considerable discrepancies, for example, between theoretical thermal conductivity values and those obtained for solid materials necessitate their re-verification for thin layers, where one dimension, i.e. thickness, is significantly smaller than the others. Due to the lack of such data for boride coatings in the literature, one of the goals of this article will be to determine them. Additionally, mechanical and thermal stability and stiffness tensors will be determined, enabling simulations of mechanical phenomena at higher computational scales. The DFT-calculated, thermal conductivity, and mechanical properties for both α- and ω-WB_2 structures of W-Al-B will then be compared with experimental results.

2. Methodology

2.1. Computational methods

2.1.1. Ab initio calculations

All ab initio calculations (relaxation of the structures, computation of cohesive energies, elastic constants, etc.) follow the methodology described in our previous work [12]. The program used for density functional theory (DFT) [34,35] and density functional perturbation theory (DFPT) [36] computations is ABINIT [37] with a local density approximation (LDA) [38] as an exchange-correlation (XC) functional and projector augmented-wave formulation (PAW) pseudopotential taken from the PseudoDojo project [39].

2.1.2. Cohesive energy and formation enthalpy

The cohesive energy and formation enthalpy of $W_{1-x}Al_xB_2$ structures were determined as follows [40,41]:

$$E_{coh}(W_{1-x}Al_xB_2) = E_{total}(W_{1-x}Al_xB_2) - (1-x)E_{iso}(W) - xE_{iso}(Al) - 2E_{iso}(B) \tag{1}$$

$$\Delta_fH(W_{1-x}Al_xB_2) = E_{coh}(W_{1-x}Al_xB_2) - (1-x)E_{coh}(W) - xE_{coh}(Al) - 2E_{coh}(B) \tag{2}$$

where: $E_{coh}(W_{1-x}Al_xB_2)$ is the cohesive energy of the $W_{1-x}Al_xB_2$; $E_{coh}(W)$ is the cohesive energy of W; $E_{coh}(Al)$ is the cohesive energy of Al; $E_{coh}(B)$ is the cohesive energy of B; $E_{tot}(W_{1-x}Al_xB_2)$ is the total energy of the $W_{1-x}Al_xB_2$; $E_{iso}(W)$ is the total energy of a W atom, $E_{iso}(Al)$ is the total energy of a Al atom and $E_{iso}(B)$ is the total energy of a B atom; $\Delta_fH(W_{1-x}Al_xB_2)$ is the formation enthalpy of the $W_{1-x}Al_xB_2$.

To calculate the cohesive energy, reference structures were chosen: for tungsten (cI2-Im-3m (229)), for aluminium (cF4-Fm-3m (225)) and for boron (hR12- R-3m (166)).

2.1.3. Mechanical properties calculations

The theoretical ground state elastic constants C_{ij} for all analyzed structures were calculated using metric tensor formulation of strain in density functional perturbation theory (DFPT) [36]. Isotropized bulk modulus B, shear modulus G, Young's modulus E and Poisson's ratio ν were estimated using a Voigt–Reuss–Hill average [42,43]. To verify the mechanical stability of all the structures, positive definiteness of the stiffness tensor was examined [44] by calculating Kelvin moduli, i.e. eigenvalues of the stiffness tensor written in second-rank tensor notation [45]. Hardness H_v and fracture toughness K_{IC} of all the $W_{1-x}Al_xB_2$ samples were estimated with the use of semi-empirical formulas developed in [46]. The Pugh ratio B/G, where B is the bulk modulus and G is the shear modulus, represents the competition between two processes, plasticity and fracture. If plasticity is easier to achieve, then a material will tend to be ductile; whereas, if fracturing is easier, then a material will tend to be brittle. Pugh [47] proposed relations between the elastic and plastic properties of pure polycrystalline metals possessing the same lattice structure. It was also demonstrated that this criterion applies to both cubic and hexagonal structures. The ratio B/G is affected by the crystal structure. However, these effects are often neglected to facilitate easy comparison of materials. The basic form of this criterion is:

$$P_u = \frac{cBa}{Gb} \tag{3}$$

where: b is the Burgers vector, c is a constant for a particular crystal structure and a is a lattice parameter. The effects of crystal structure can be neglected if b/ac is constant in an investigated group of materials. Hence, the ratio B/G provides a measure of the likely nature of a material's failure: a low value of B/G implies brittle failure, while a high value implies ductile failure. This assumes that the changes in crystal structure affect both processes equally. For boride films, this assumption was verified in [11]. The obtained results for the Pugh ratio were compared with two other theories, the Frantsevich criterion (regarding Poisson's ratio ν) and the Cauchy pressure (C_{12}-C_{44}) - Pettifor criterion. Good compliance was obtained, and a ductile behaviour for borides was established for $B/G < 1.75$. Plastic index [48] of hard nanocomposite coatings was estimated by the H_v/E ratio, where $E^* = E/(1 - \nu^2)$.

2.1.4. Thermal conductivity

For the empirical estimation of thermal conductivity, the Clarke model [49] and the Cahill–Pohl model [50] were used. Both methods are presented and compared in [30].

2.2. Experimental methods

2.2.1. Magnetron sputtering

The study employed silicon substrates Si(100) on which $W_{1-x}Al_xB_z$

(x = 0–1) thin films were deposited using the combined HiPIMS-DC magnetron sputtering method. The deposition process was carried out in a vacuum chamber, which was evacuated to a base pressure of 4×10^{-4} Pa and then filled with argon to a working pressure of 0.9 Pa. During deposition, two magnetron modules (PREVAC MS2 63C1) with a DC and HiPIMS power supply were used. The pulse parameters of HiPIMS with τ = 200 μs and frequency f = 700 Hz were optimazed using a process that accounted for coating stoichiometry, mechanical properties, and deposition rate, as fully described in work [51]. The $W_{1-x}Al_xB_z$ films were deposited using two targets: SPS sintered $AlB_{2.5}$ and commercially available W_2B_5 (99.5 % purity, Kurt J. Lesker). In the case of $AlB_{2.5}$ target, aluminium (99.5 % purity, average grain size 25–35 μm, Sigma Aldrich), and amorphous boron (95 % purity, average grain size 1 μm) powders in the (W+Al)/B molar ratio of 1/2.5 were mixed for 30 min using a Turbula® T2F shaker-mixer (WAB, Switzerland). Afterwards, the received material was placed in the HP D 25/3 (FCT Systeme, Germany) sintering press. More information about the sintering process can be found in the authors previous papers [52]. The deposition rate from each target was individually controlled. First, the sputtering process rate had to be determined. For this purpose, a quartz balance (Quartz Thickness Monitor) built into a vacuum chamber was used for measurement, where the sputtering rate was determined by reading the instantaneous value directly from the quartz balance. Table 1 presents the individual parameters for each sample, including the targets types, deposition method, power and target-substrate distance. The deposition time for all samples was 120 min, with a substrate temperature of 400 °C, and a DC negative bias voltage of 50 V. Before deposition, the substrates' were cleaned in an ultrasonic bath with deionized water and then in acetone. After that, substrates were plasma cleaned by applying a −600 V DC bias voltage for 15 min.

2.2.2. Characterization

To determine the density $ρ$ of the films, it was necessary to establish their mass and volume. The mass increase of the film relative to the substrate was determined using an analytical balance (Radwag MXA11/1), with a maximum mass of 11 g, and a resolution of 1 μg. The mass of the coatings m was determined by measuring the difference in the mass of the silicon substrates before and after deposition. The final mass was obtained as the average of ten measurements. To determine the volume, the coating's thickness h was determined from cross-section SEM images. The surface area s of the deposited film on a 10 × 10 mm silicon wafer was measured with an optical microscope. The density was calculated using the well-known formula $ρ = m/(h•s)$.

Scanning electron microscopy (SEM) investigations were conducted using a ThermoFisher Scientific™ Helios™ 5 UX device equipped with a focused ion beam (FIB) lift-out technique. The SEM images of the deposited films' surface were acquired in the secondary electron mode. The samples for transmission electron microscopy (TEM) investigations were prepared using the FIB technique with Ga^+ ions. Cross-sections were observed using scanning transmission electron microscopy (STEM-in- SEM mode) to measure film thickness. The TEM investigations of prepared lamellae were carried out using a JEOL JEM F200 TEM microscope operating at 200 kV. Bright-field images with corresponding selected area electron diffraction (SAED) patterns were acquired

The topography was scanned in contact mode using a FlexAFM (Nanosurf AG) atomic force microscope (AFM) equipped with a HQ: CSC17/Cr-Au BS probe. The normal load was equal to a few tens of nanonewtons, and the scanning speed was 1.3 μm/s for 1 × 1 μm areas. The obtained data were analyzed using the Gwyddion open-source software [53]. Raw images were leveled by mean plane subtraction and removing polynomial background.

The X-Ray Diffractometry was carried out using a Bruker D8 Discover in 2θ scan mode, with Cu-Kα radiation (λ=0.15418 nm). The XRD patterns were obtained with the incidence angle fixed at 8° position. This position was chosen to reduce the signal from the substrate while maintaining the high intensity of the signal originating from the coating. After indexing the XRD pattern, the lattice constant was calculated using Bragg's law (and Miller indices).

Due to the low accuracy of the standard SEM-EDS method during chemical composition measurements for light elements such as boron, the TOF-ERDA method was used to determine the elemental composition. Recoils are generated using 23 MeV $^{127}I^{7+}$ ions with an angle of incidence of 20° on the sample surface. The TOF-ERDA spectrometer was positioned at an angle of 37.5° toward the beam direction.

2.2.3. Mechanical properties

The deposited coatings were examined in terms of hardness and Young's modulus. The Berkovich indenter was loaded and unloaded at a rate of 1 mN/s up to the peak load of 10 mN, with a dwell time of 2 s. At least 15 valid indents on each coating were evaluated. The hardness was measured by the peak load and the projected area of the indenter during indentation, and the reduced Young's modulus was determined using the Oliver-Pharr method [54]. The load was selected so that the maximum penetration depth during measurement did not exceed 10 % of the coating thickness, thereby avoiding the substrate influence. According to theory, the elasticity modulus should be measured with the lowest possible load. Therefore, Young's modulus values were measured at a load of 2 mN. To evaluate the relative nanoindentation toughness of the films, testing was conducted to determine their resistance to crack propagation under tensile loading with a load of 150 mN, quantified by the critical stress intensity factor (K_{IC}). Standardized procedures were followed, using FESEM-FIB ZEISS Crossbeam 350 to accurately measure the imprint dimensions and length of cracks made with a sharp diamond cube corner indenter. The K_{IC} values were calculated using Eq. (4) [55].

$$K_{IC} = δ\left(\frac{E}{H}\right)^{0.5} \frac{F_m}{c_K^{1.5}} \tag{4}$$

where: $δ$–indenter geometry factor, F_m – the indentation load and c_K - length from the centre of the indent to the end of the crack.

2.2.4. Thermal conductivity

The thermal conductivity of AlB_2-$WB_{2.5}$ layers was measured using the Netzsch Nano-TR apparatus. The device uses the thermoreflectance method, in which the change in reflected light caused by a temperature change is measured. Measurements were performed in the front-heating and front-detection mode (FF), which is particularly useful for thin layers on non-transparent substrates [56]. Although this method allows for the measurement of various types of layers (metallic or ceramic), it

Table 1
HiPIMS-DC magnetron sputtering deposition parameters of $W_{1-x}Al_xB_z$ (x = 0–1) layers.

Sample	Target 1	Power supply	Power (W)	Target-Substrate Distance (mm)	Target 2	Power supply	Power (W)	Target-Substrate Distance (mm)
#1	W_2B_5	HiPIMS	250	80	-	-	-	-
#2	W_2B_5	HiPIMS	250	80	$AlB_{2.5}$	DC	100	140.5
#3	W_2B_5	HiPIMS	250	80.5	$AlB_{2.5}$	DC	120	140.5
#4	W_2B_5	HiPIMS	200	110	$AlB_{2.5}$	DC	140	130.5
#5	W_2B_5	DC	100	120	$AlB_{2.5}$	HiPIMS	200	80.5
#6	W_2B_5	DC	70	120	$AlB_{2.5}$	HiPIMS	270	80
#7	-	-	-	-	$AlB_{2.5}$	HiPIMS	270	80

has its limitations. It is extremely sensitive to heterogeneity in the chemical composition of layers, the presence of porosity in the structure, or its anisotropy, and at the same time requires a very high surface smoothness of the tested materials [57,58]. The samples before testing were covered with a thin (~100 nm) molybdenum film (heat capacity c_p = 249 J/(kg·K), density ρ = 10.20 g/cm^3) as an anti-reflection coating deposited by sputtering. The technical parameters of the measurements were as follows: wavelength 1545 nm, pulse width 1 ns, number of pulses 100 000, pulse repetition frequency 50 kHz, output peak power 8.4 kW and output power during FF operation 110 mW. The beam divergence was 30°. The experimental thermoreflectance curve is compared with the theoretical curve obtained from the "Nano-TR Thermal Simulator". It performs simulations by varying the thermal conductivity of the layer to be measured. The thermal conductivity with the smallest difference between the simulation result and the measured value is calculated as the optimum value. To perform the measurement, it was necessary to input the thickness and density values into the software and provide the specific heat capacity of the studied materials. The specific heat capacity was determined from the literature [59]. The heat capacity of alloyed films was calculated using mixing rules based on the measured amount of Al and W. Additionally, the thickness and density of the films were assumed based on experimental values determined within this study, and for Si substrate, density ρ = 2.33 g/cm^3 and c_p = 711 J/(kg·K) were used.

3. Results

3.1. DFT calculations

Tungsten boride crystallizes in various phases and ω-WB$_2$ P6$_3$/mm (Fig. 1a) appears to be the hardest, however it is mostly synthesized as bulk material, for example, by SPS sintering [52]. However, α-polymorph dominates in our experimental samples, and in the case of α-WB$_2$ P6/mmm (191), (Fig. 1b), it can form thin films by deposition with PVD methods [11]. When considering AlB$_2$, only the P6/mmm hexagonal polymorph is known to be a stable structure. Therefore, in the omega structure, the calculation ends with a 50 % aluminium to tungsten ratio. Table 2 shows how the addition of aluminium affects the thermodynamical properties and density of ω-WB$_2$ P6$_3$/mmc (194) phase (Fig. 1a) and α-WB$_2$ P6/mmm (191) phase (Fig. 1b). Also replacement of the Al

by W atoms in α-AlB$_2$ P6/mmm (191) phase (Fig. 1c) was verified and results of ab-initio calculations are also presented in Table 2. All obtained values of the formation enthalpy ΔH_f are negative, which means that all calculated structures are thermodynamically stable.

To conduct the calculations, the following supercells of ω-WB$_2$ were generated: 2 × 1 × 1 (12 atoms), 3 × 1 × 1 (18 atoms), 2 × 2 × 1 (24 atoms), 3 × 2 × 1 (36 atoms), 2 × 2 × 2 (48 atoms), 3 × 3 × 1 (54 atoms), 3 × 2 × 2 (72 atoms), 4 × 4 × 1 (96 atoms) and 2 × 2 × 1 defected with WB$_2$ cluster (24–3 = 21 atoms). For α-WB$_2$ and α-AlB$_2$, the supercells were: 2 × 2 × 1 (12 atoms), 2 × 2 × 2 (24 atoms), 3 × 3 × 1 (27 atoms), 3 × 2 × 2 (36 atoms), 3 × 3 × 2 (54 atoms), 3 × 3 × 3 (81 atoms) and 2 × 2 × 2 defected with WB$_2$ cluster (24–3 = 21 atoms); one arbitrary tungsten atom was replaced with a aluminium atom. In the two structures with defects, a cluster of three atoms was removed, i.e. a triple defect consisting of a W atom and two B atoms; such a defect does not alter the chemical composition of the metal and the boron. It was observed by X. Zhu et. al. [60] that a cluster of defects modifies the hardness of pure Al more than uniformly distributed defects. Examples of the generated supercells are shown in Figs. S1a and S1b (supplementary materials). It did not matter which W atom was replaced by Al because they are equivalent. However, the doped structure has a different symmetry than that of the original WB$_2$ or AlB$_2$ (see Table 2). The generated structures were then fully optimized, in terms of cell geometry and atomic coordinates, as in the authors' previous work [61].

The calculated Kelvin moduli, i.e. the eigenvalues of the stiffness tensor, for all analyzed structures are given in Table S1 (supplementary materials). It can be found that the values for each sample are positive. This means that all of the structures are also mechanically stable.

The DFT results for mechanical properties and thermal conductivity are presented in Table 3. The two WB$_2$ structures have comparable theoretical values for density and thermal conductivity. In all cases, introducing a defect reduces their values. Regarding mechanical properties, the ω-WB$_2$ structure has higher values. However, the addition of aluminium results in a significant decrease in their values. The case is different for the α-WB$_2$ structure, where the theoretical hardness of about 20 GPa is maintained for a dopant content of 0–50 % aluminium. It is comparable to introducing a defect into both structures, resulting in a slight increase in hardness for α-WB$_2$ and a decrease from 30 GPa to 15 GPa for ω-WB$_2$. A two-fold decrease to 300 GPa also occurs for the Young's modulus for the defected structure.
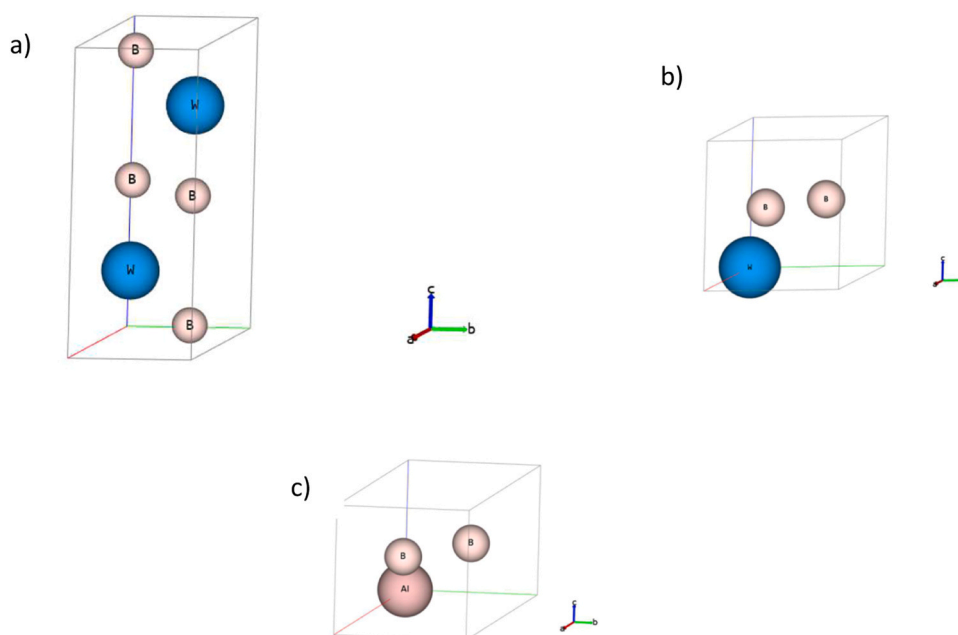

Fig. 1. Theoretical boride basic cells: a) WB$_2$-hP6-P6$_3$/mmc (194), b) WB$_2$-hP3-P6/mmm (191), c) AlB$_2$-hP3-P6/mmm (191).

Table 2

DFT calculations results of W-Al-B coatings cohesive energy and formation enthalpy: chemical formula; space group; Pearson symbol; proportion of Al dopant: x = Al/(W +Al); Volume per atom (Å^3/Atom); formation enthalpy ΔH_f (eV/Atom); cohesive energy E_c (eV/Atom); density ρ (g/cm^3); open markers refer to structures with a defect.

Sample	Space group	Pearson symbol	Al/(Al+W)	Vol/atom	- ΔHf	-Ec	ρ
hP6							
WB2	P63/mmc (194)	hP6	0/1	9.298	0.422	8.88	12.231
W0.5Al0.5B2	P-6m2 (187)	hP6	1/2	9.295	0.172	7.091	7.564
W0.75Al0.25B2	Pmm2 (25)	oP12	1/4	9.27	0.206	7.894	9.926
W0.835Al0.165B2	Pm (6)	mP18	1/6	9.276	0.265	8.21	10.7
W0.875Al0.125B2	Amm2 (38)	oC24	1/8	9.255	0.289	8.363	11.115
W0.915Al0.085B2	Pm (6)	mP36	1/12	9.262	0.322	8.524	11.498
W0.937Al0.063B2	Amm2 (38)	oC48	1/16	9.27	0.338	8.604	11.683
W0.944Al0.056B2	Amm2 (38)	oC54	1/18	9.265	0.345	8.632	11.754
W0.958Al0.042B2	Pm (6)	mP72	1/24	9.268	0.356	8.686	11.88
W0.969Al0.031B2	Amm2 (38)	oC96	1/32	9.271	0.363	8.726	11.974
W0.857Al0.143B2∘	P1 (1)	aP21	1/7	10.451	0.023	7.995	9.695
hP3							
WB2	P6/mmm (191)	hP3	0/1	8.918	0.227	8.685	12.752
W0.5Al0.5B2	P6/mmm (191)	hP6	1/2	8.407	0.142	7.06	8.364
W0.75Al0.25B2	P6/mmm (191)	hP12	1/4	8.523	0.252	7.941	10.797
W0.875Al0.125B2	P6/mmm (191)	hP24	1/8	8.518	0.128	8.201	12.076
W0.889Al0.111B2	P6/mmm (191)	hP27	1/9	8.521	0.126	8.242	12.214
W0.915Al0.085B2	P2/m (191)	mP36	1/12	8.53	0.141	8.342	12.484
W0.944Al0.056B2	P6/mmm (191)	hP54	1/18	8.558	0.129	8.416	12.725
W0.963Al0.037B2	P6/mmm (191)	hP81	1/27	8.583	0.132	8.476	12.875
W0.857Al0.143B2△	P1 (1)	aP21	1/7	9.189	0.192	8.21	11.027
hP3							
AlB2	P6/mmm (191)	hP3	1/1	8.242	0.073	5.451	3.264
W0.5Al0.5B2	P6/mmm (191)	hP6	1/2	8.407	0.142	7.06	8.364
W0.25Al0.75B2	P6/mmm (191)	hP12	3/4	8.27	0.071	6.219	5.878
W0.125Al0.875B2	P6/mmm (191)	hP24	7/8	8.282	0.086	5.849	4.558
W0.111Al0.889B2	P6/mmm (191)	hP27	8/9	8.248	0.074	5.794	4.431
W0.085Al0.915B2	P2/m (10)	mP36	11/12	8.275	0.081	5.716	4.125
W0.056Al0.944B2	P6/mmm (191)	hP54	17/18	8.254	0.079	5.628	3.844
W0.037Al0.963B2	P6/mmm (191)	hP81	26/27	8.244	0.079	5.571	3.653
W0.143Al0.857B2□	P1 (1)	aP21	6/7	9.16	0.032	5.786	4.291
W	Im-3m (229)	cI2		15.491		12.859	19.707
Al	Fm-3m (225)	cF4		15.924		3.617	2.814
B	R-3m (166)	hR12		20.947		6.258	2.571

3.2. Microstructure and chemical composition

Table 4 presents the results of the chemical composition analysis of the deposited W-Al-B films. In all deposited layers, there is an excess of boron compared to the stoichiometric amount of the compound. This is caused by the dynamics of the magnetron-induced plasma. Boron ions move perpendicularly to the target surface, while aluminium is more dispersed [3,21]. Additionally, this is related to the excess of boron in the sputtered targets W_2B_5 and $AlB_{2.5}$, respectively.

The results so far have usually shown a boron deficiency. However, the HiPIMS method also causes ionization of the sputtered material atoms. The use of substrate polarization attracts these ions to the substrate, leading to lower losses. In addition, impurities such as hydrogen, carbon, nitrogen and oxygen (standard impurities of the sputtering target and generated during sample transport) and argon, the working gas during the deposition process, can be observed in the films. The amount of argon can have a significant effect on the residual stresses in the films, however its amount in the deposited films is relatively small, due to their high density. In the case of oxygen, its amount increases with the amount of aluminium, which is related to the very high negative enthalpy related to the formation of the Al_2O_3 compound ($\Delta H_f = -3.427$ eV/atom). This causes the residual oxygen to be easily bound by aluminium. In the rest of the article, the amount of aluminium (AlAl + W) will be denoted by x and the amount of boron in deposited films by $2+z$.

In Fig. S2 (supplementary materials) sample surfaces and cross-sections observed using a STEM technique are shown. Increasing the amount of aluminium decreases the film thickness. This phenomenon is related to the dynamics of the plasma [9]. Scattering in directions other than perpendicular to the substrate, combined with the lower atomic mass of aluminium, causes WB_x films (deposited in 120 min) to be approximately four times thicker than the layers with a high aluminium content or AlB_x

AFM measurements of the sample surface topography (Fig. 2) show a low roughness of the samples. The maximal height of grains ranging between 23.8 nm for the sample without aluminum and 6.6 nm for the sample without tungsten. With increasing aluminum content, the diameter of the surface grains decreases. In the case of sample #7 (x = 100 %), the sample is smooth and shows no graininess.

With increased aluminium content, the surface morphology and cross-sectional structure of the films also vary. In sample WB_2 (sample #1), a slight roughness is observed. This results from the partially columnar structure (Fig. 2a). The addition of 1.4 % Al makes the structure become more ordered, allowing a columnar structure to be observed. In this case, the cross-sectional bright-field TEM image shows characteristic V-shaped grains (Fig. 2b), and a more coarse-grained surface microstructure. In the case of 7.3 % aluminium, a decrease in roughness is observed, which may be related to the more fine-grained microstructure and a reduction in column thickness. Additionally, the grain arrangement changes. In this case, they form a columnar structure, in which the grains grow perpendicular to the substrate (Fig. 2c). Further increases in the dopant amount result in the formation of an amorphous phase. The observations carried out are consistent with the model proposed by Barna and Adamik [62]. Aluminium atoms can be

Table 3

DFT calculations results of W-Al-B coatings mechanical properties: Chemical formula; Bulk modulus B (GPa); shear modulus G (GPa); Young's modulus E (GPa); Poisson's ratio ν; B/G Pugh's ratio; hardness H_v (GPa); hardness to modified Young's modulus ratio H_v/E^*; fracture toughness K_{IC} (MPa$\sqrt{m}$); thermal conductivity κ_{min} (W/(m•K)) (open markers: ○, △, □ refer to structures with a defect).

Sample	B	G	E	ν	B/G	H_v	H_v/E^*	K_{IC}	κ_{min}
ω- WB_2 hP6									
WB_2	336.64	258.99	618.4	0.19	1.3	34.27	0.053	5.46	2.015
$W_{0.5}Al_{0.5}B_2$	246.75	98.27	260.25	0.32	2.51	14.16	0.049	2.52	1.695
$W_{0.75}Al_{0.25}B_2$	282.03	190.31	466.1	0.22	1.48	21.81	0.044	3.86	1.948
$W_{0.835}Al_{0.165}B_2$	300.79	208.62	508.34	0.22	1.44	24.3	0.045	4.32	1.958
$W_{0.875}Al_{0.125}B_2$	325.59	251.71	600.41	0.19	1.29	33.56	0.054	5.21	2.089
$W_{0.915}Al_{0.085}B_2$	317.61	240.36	575.82	0.2	1.32	31.01	0.052	4.94	2.01
$W_{0.937}Al_{0.063}B_2$	322.14	245.41	587.13	0.2	1.31	31.98	0.052	5.08	2.013
$W_{0.944}Al_{0.056}B_2$	322.92	247.97	592.3	0.19	1.3	32.71	0.053	5.12	2.016
$W_{0.958}Al_{0.042}B_2$	325.6	251.72	600.43	0.19	1.29	33.56	0.054	5.21	2.019
$W_{0.969}Al_{0.031}B_2$	328.68	256.29	610.25	0.19	1.28	34.63	0.055	5.32	2.027
$W_{0.857}Al_{0.143}B_2$○	175.48	124.72	302.5	0.21	1.41	14.84	0.047	1.99	1.465
α- WB_2 hP3									
WB_2	338.6	156.06	405.83	0.3	2.17	21.18	0.047	4.28	1.664
$W_{0.5}Al_{0.5}B_2$	269.07	180.98	443.5	0.23	1.49	20.72	0.044	3.53	2.209
$W_{0.75}Al_{0.25}B_2$	320.38	137.29	360.38	0.31	2.33	19.25	0.048	3.79	1.762
$W_{0.875}Al_{0.125}B_2$	348.19	155.36	405.73	0.31	2.24	21.41	0.048	4.37	1.765
$W_{0.889}Al_{0.111}B_2$	318.04	123.23	327.39	0.33	2.58	17.91	0.049	3.59	1.588
$W_{0.915}Al_{0.085}B_2$	319.1	133.96	352.54	0.32	2.38	18.94	0.048	3.74	1.622
$W_{0.944}Al_{0.056}B_2$	346.96	143.85	379.15	0.32	2.41	20.43	0.048	4.22	1.663
$W_{0.963}Al_{0.037}B_2$	341.57	133.45	354.23	0.33	2.56	19.34	0.049	4.02	1.6
$W_{0.857}Al_{0.143}B_2$△	297.8	192.64	475.4	0.23	1.55	21.89	0.044	4.1	1.879
α- AlB_2 hP3									
AlB_2	199.4	169.05	395.41	0.17	1.18	25.96	0.064	2.64	3.379
$W_{0.5}Al_{0.5}B_2$	269.07	180.98	443.5	0.23	1.49	20.72	0.044	3.53	2.209
$W_{0.25}Al_{0.75}B_2$	233.64	125.86	320.09	0.27	1.86	15.61	0.045	2.58	2.276
$W_{0.125}Al_{0.875}B_2$	214.23	128.84	321.98	0.25	1.66	14.94	0.044	2.38	2.581
$W_{0.111}Al_{0.889}B_2$	214.52	132.93	330.51	0.24	1.61	15.23	0.043	2.41	2.658
$W_{0.085}Al_{0.915}B_2$	207.88	125.32	313.06	0.25	1.66	14.52	0.044	2.27	2.677
$W_{0.056}Al_{0.944}B_2$	203.78	124.71	310.75	0.25	1.63	14.35	0.043	2.22	2.767
$W_{0.037}Al_{0.963}B_2$	202.86	126.91	315.03	0.24	1.6	14.5	0.043	2.23	2.858
$W_{0.143}Al_{0.857}B_2$□	179.45	111.71	277.53	0.24	1.61	12.78	0.043	1.88	2.308

Table 4

Chemical composition of deposited W-Al-B films.

ToF-ERDA [% at.]										
Sample	H	B	C	N	O	Al	Ar	W	Al/Al+W	B/Al+W
#1	0.25	65	0.50	0.15	0.90	0	1.1	31.0	0	2.09
#2	0.24	68	1.50	0.50	0.14	0.4	0.7	28.0	0.014	2.39
#3	0.13	69	0.60	0.30	2.00	1.8	1.3	23.0	0.073	2.78
#4	0.12	66	1.10	0.30	3.20	5.4	1.4	22.0	0.197	2.40
#5	0.21	64	2.20	0.90	3.10	14.7	0.9	13.0	0.531	2.31
#6	0.20	68	1.20	0.80	3.70	17.9	0.7	7.2	0.713	2.71
#7	0.57	67	0.86	0.57	5.90	25.0	0.1	0	1.000	2.68

considered as impurity species that hit the film surface, which are then dissolved into the crystal lattice or adsorbed and segregated on the surfaces of growing crystals. In small amounts, aluminium can act as a promoter, facilitating crystal growth and increasing grain size. Further increase in the amount of aluminium changes its role to an inhibitor. In the case studied, active impurities in the form of excess aluminium atoms (x > 7.3 %) can inhibit the basic structure-forming phenomena by reducing the grain size and weakening texture [62]. At high levels of aluminium concentration, crystal growth is periodically blocked by the second phase (α-AlB$_2$). It means that grain growth cannot occur, which also hinders the development of the restructuring growth texture and, consequently, the formation of the amorphous phase in the films. As shown by DFT calculations, the α-AlB$_2$ structure has a relatively low negative formation enthalpy (0.073 eV/atom), which requires a higher energy input during deposition. The associated higher mobility of adatoms enables the crystal lattice to be ordered, facilitating the transition from the amorphous to the columnar crystalline phase. The use of the HiPIMS method with high-energy plasma partially solves this problem;

however, to obtain a crystalline film, it is necessary to heat the substrate during deposition to temperatures significantly higher than 400 °C [18]. In the case of WB$_2$, the negative formation enthalpy is much higher, which causes the growth of crystalline layers to begin at a temperature of 400 °C, even with a small amount of aluminium. It is confirmed by XRD studies and SAED patterns. Fig. 4 shows the spectra recorded for individual samples.

In the case of low aluminium content (samples #2 and #3), a dominant peak can be observed at an angle 2θ of 28.8°, corresponding to the 001 direction. Further increasing the aluminium content leads to amorphization of the film. Comparison of the 001 peak position across different aluminium contents does not show significant shifts. The Rietveld analysis was carried out for aluminium contents 1.4 % and 7.3 %. However, due to the presence of only one visible peak in the recorded XRD pattern, the fitting quality is limited. The parameters obtained from the Rietveld refinement are: a = 3.015 Å and c = 3.179 Å. Additionally, calculations of the lattice parameter of the α-WB$_2$ phase for samples #2 and #3 were performed based on the SAED patterns.
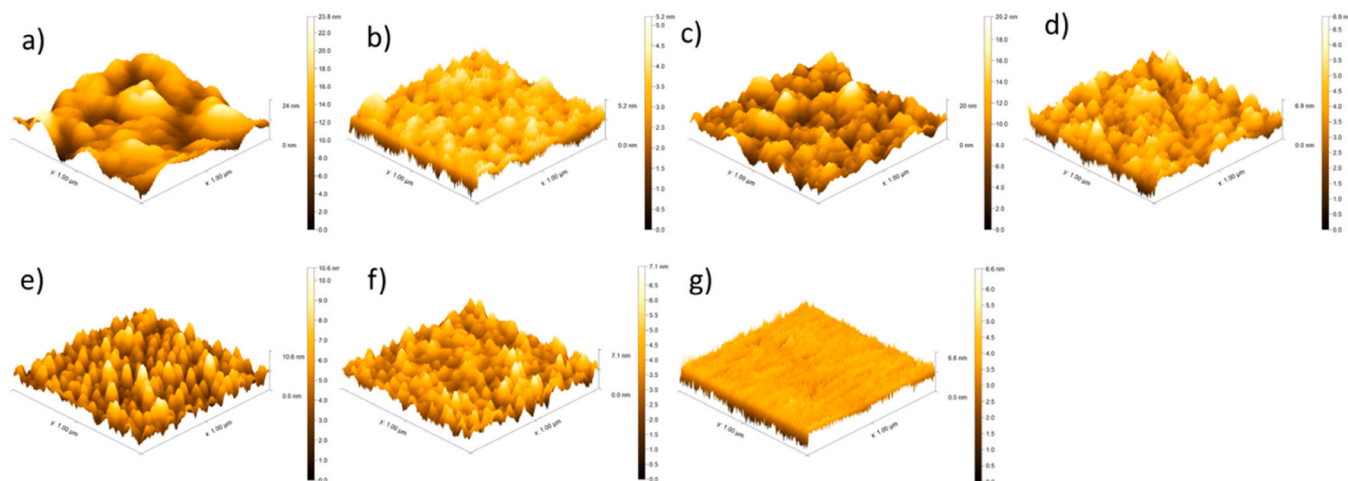
Fig. 2. AFM images of surface topography acquired from films (a) x = 0, (b) 1.4 %, (c) 7.3 %, (d) 19.7 %, (e) 53.1 % (f) 71.3 % and (g) x = 100 % of aluminium. Measurement area 1 × 1 μm.

Calculation of parameters "a" and "c" was performed using (100) and (001) planes, respectively. The parameter "a" is in the range of 3.094 and 3.098 Å, and the parameter "c" is in the range of 3.170 and 3.185 Å. Both parameters are relatively in good agreement with XRD measurements. However, it should be noted that XRD determination of the lattice parameter is significantly more accurate than calculation from SAED. According to the literature, the accuracy of measurements of interplanar spacing and the resulting lattice parameter based on SAED could be in the order of a few percent. Williams and Carter [63] evaluated the accuracy of lattice parameter determination from SAED to be up to 3 %. The experimental results are relatively consistent with the calculations, where for α-WB$_2$ P6/mmm the crystalline constants are a = 3.002 Å and c = 3.318 Å, respectively. The lattice parameters depend on the amount of boron in the compound under consideration. According to calculations carried out by Fuger et al. [33], an increase in the boron excess to W/B= 2.5 (Table 4) causes a decrease in the lattice

constant c, while the parameter a remains practically unchanged. In undoped samples (samples #1 and #7), in addition to the amorphous base, additional peaks can be observed in characteristic places of the α-WB$_2$ and α-AlB$_2$ phases, respectively. A similar phenomenon can be observed in SAED patterns, where, in addition to the amorphous halo, clear spot reflecting the crystal lattice are visible (Fig. 3a, g). Such a system results from the too low energy of the deposited particles, an increase in their energy would ensure the formation of the crystal structure. The SAED patterns with rings that represent sets of planes are presented in figure S3 in the supplementary materials.

3.3. Density

In works describing thin films made of transition metal borides, one can very often find a statement that the coatings are dense. Such an effect is mainly observed in the HiPIMS method, where the high energy
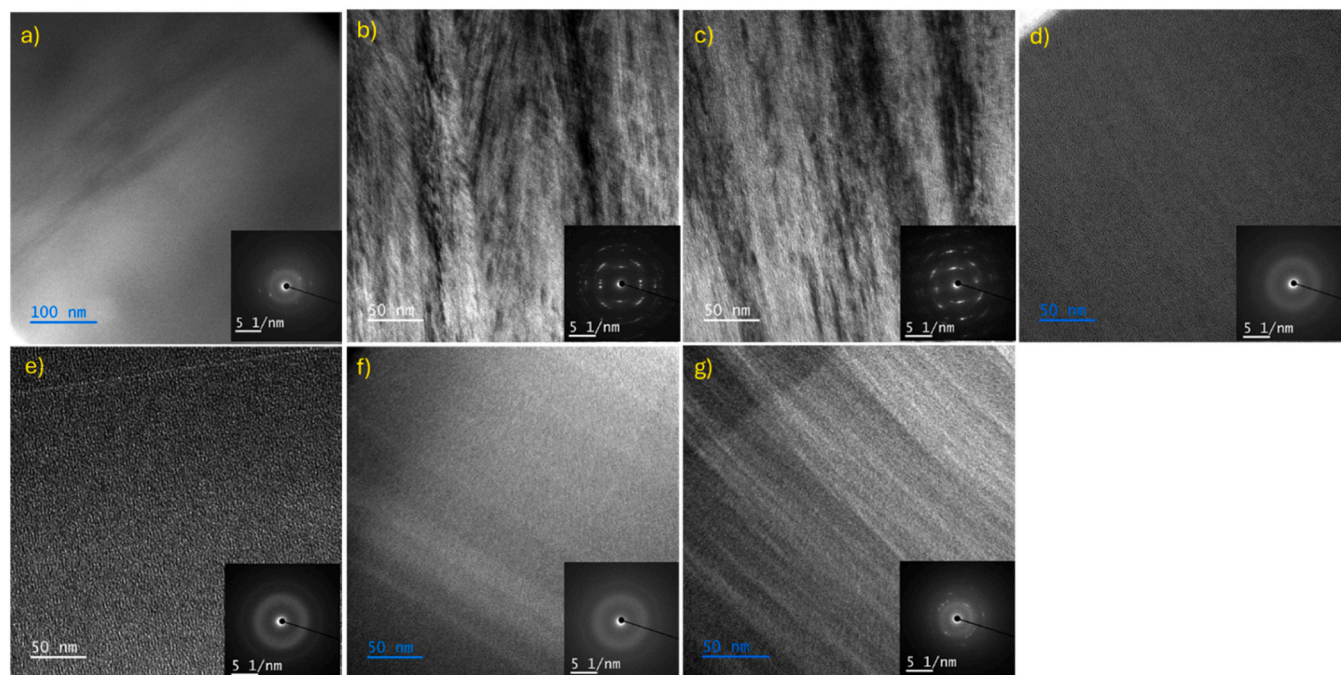

Fig. 3. Cross-sectional bright field TEM images with corresponding SAED patterns acquired from films (a) x = 0, (b) 1.4 %, (c) 7.3 %, (d) 19.7 %, (e) 53.1 % (f) 71.3 % and (g) x = 100 % of aluminium.

of the plasma cloud increases the surface diffusion of adatoms. In this case, atoms more easily occupy their positions in the crystal lattice, resulting in less defective films. Additionally, bombardment with heavy atoms such as tungsten or tantalum further densifies the coatings and enhances their subsequent hardening [64]. However, there is little information about the actual density of such films. Fig. 5 compares the densities determined both theoretically and experimentally.

The increase in aluminium results in a significant decrease in the density of the layers, from 11.1 g/cm^3 to 3.3 g/cm^3 for films without tungsten. Such a phenomenon is evident because much lighter aluminium atoms replace heavier tungsten atoms. The determined density values for the P6/mmm structure are higher than for the P6$_3$/mmc structure, which results from the arrangement of boron atoms in the tested WB$_2$ polymorphs. The P6/mmm structure consists of close-packed layers of metals, with boron occupying trigonal prismatic interstitial sites. This results in a layered structure along the [001] direction (Fig. 4) of alternating metal and graphite-like boron planes, which are restabilized by charge transfer from tungsten or aluminium. Additionally, tungsten can be an exception to this rule, forming more complex structures with the W$_2$B$_5$ stoichiometry, where every second boron plane is puckered. The reason for this lies in the electronegativity: tungsten is significantly more electronegative than aluminium, resulting in a significantly reduced charge transfer from the metal to the B planes [32].

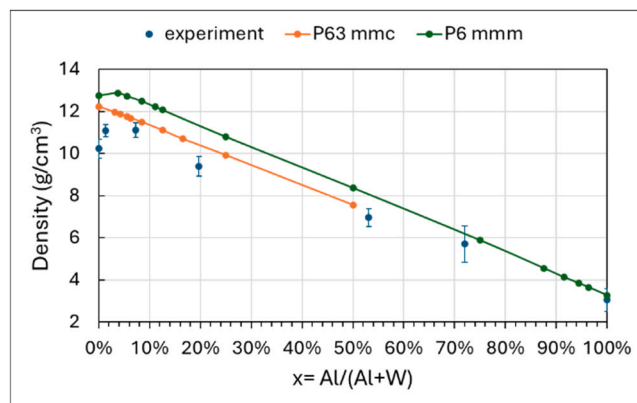A comparison of experimental and theoretical densities shows that

Fig. 5. Density of deposited W-Al-B films vs. theoretical values of α-WB$_2$, α-AlB$_2$ (P6/mmm) and ω-WB$_2$ (P6$_3$/mmc) structures.

the experimental values are lower. It is related to the excess of boron relative to the stoichiometric composition, structural defects and amorphous structure of the coatings. It can also be observed that these differences increase with increasing film thickness and, consequently, the number of defects.
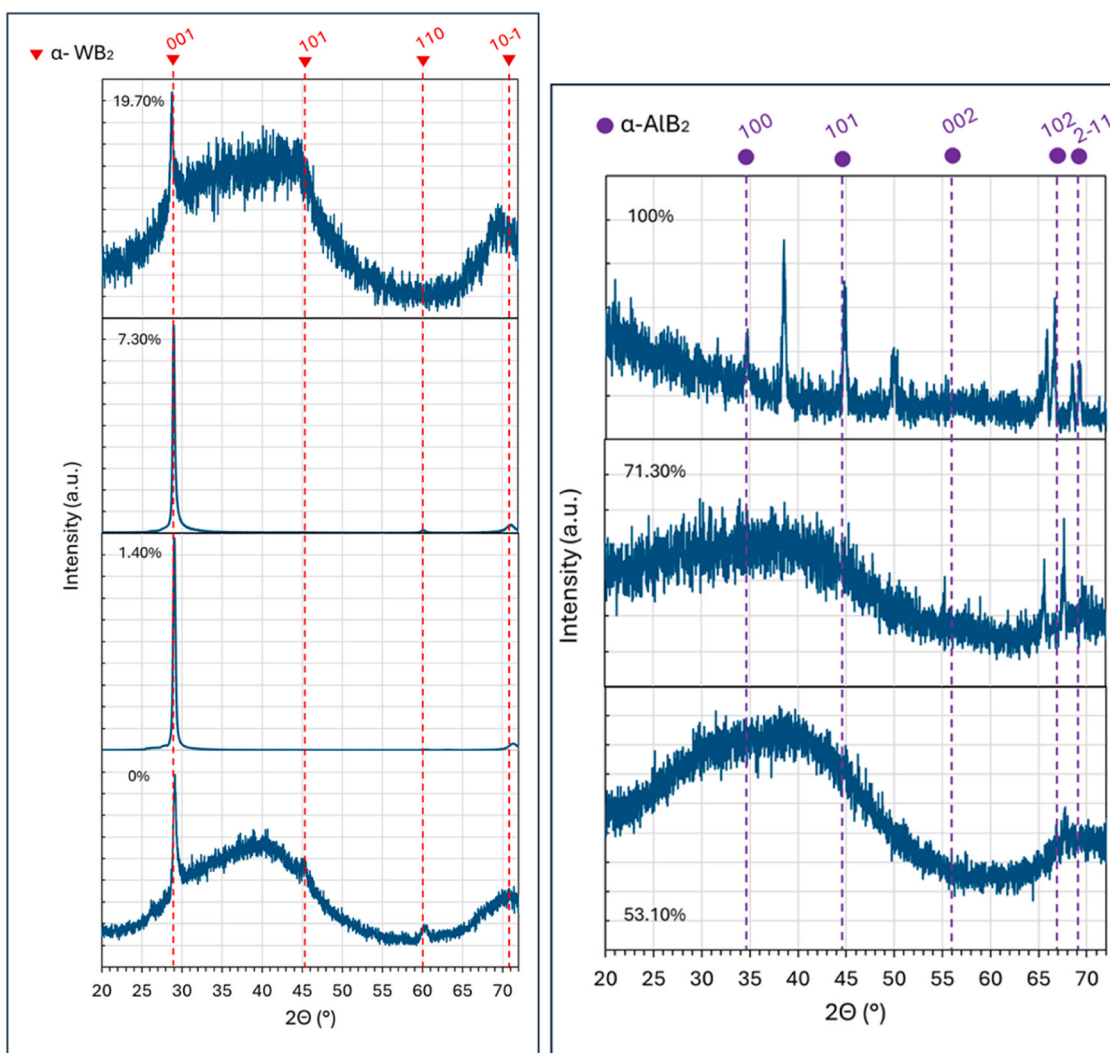

Fig. 4. XRD pattern of deposited W-Al-B films with aluminium amount x = 0–100 % deposited at a temperature of 400 °C.

3.4. Thermal conductivity

Fig. 6 shows a comparison of thermal conductivity values for theoretical P6/mmm and P6$_3$/mmc structures and the results of experimental measurements.

Both theoretical structures exhibit similar conductivities, κ min, ranging from 1.7 to 2.1 W/m•K in the aluminium content range of 0–75 %. Further calculation results show an increase in conductivity with increasing aluminium content. The highest conductivity is 3.3 W/m•K for AlB$_2$ (sample #7).

In the basic structure of TMB$_2$, the boron atoms form "graphite-like" honeycomb sheets with covalent bonding. These sheets are separated by metal atoms in hexagonal prismatic voids, characterized by metallic bonding. The character of the interlayer bonding between Al or W and boron sheets in P6/mmm structure was reported to be primarily ionic, mixed with covalent character [65], although the high electrical conductivity in the a-b plane implies metallic bonding between B and Al or W. This bond arrangement also affects the films' thermal conductivity.

The experimental results are slightly higher, but are in good agreement with the calculations. The 0 % sample #1 is amorphous and has lower boron content, but is close to the stoichiometric value, which may result in fewer defects and barriers. As a result, this causes better conductivity. Additionally, samples #6 and #7 (x = 71.3 % and 100 %) are amorphous and the thinnest, which may cause significant differences between theoretical and actual conductivity. The results closest to the theory are those for samples whose XRD patterns (Fig. 3) indicate their crystalline character. For all samples with an aluminium content of up to x = 53 %, the target containing tungsten was sputtered using the HiPIMS generator, which caused ionization of the sputtered material. In combination with the high atomic mass of tungsten, this led to a higher density of layers. Reducing the number of defects, e.g. porosity, improves heat conduction. To date, no results are available regarding the measurements of the thermal conductivity of ternary transition-metal borides in thin film form. κ$_{min}$ of WB$_2$ obtained based on Cahill's model [50] by Yang et al. [66] and Li et al. [30] are in the range of 1.663–1.927 W/m•K, which is in good agreement with the results obtained in this work. In the case of AlB$_2$ (<1 mm^2) single crystals measured with time-domain thermoreflectance (TDTR) [67], the result of the in-plane thermal conductivity was 52 ± 7 W/m•K. This result, as well as the experimental conductivity value for W$_2$B$_5$ of ~ 45 W/m•K [29], significantly differs from the theoretical values and may be due to different types of atomic bonds and to the microstructure at a higher dimensional scale, compared to the studied films.

3.5. Mechanical properties

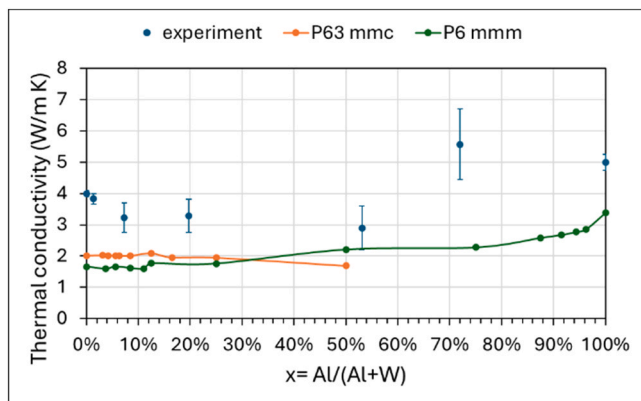Theoretical calculations of mechanical properties show (Fig. 7) that

Fig. 6. Thermal conductivity of deposited films vs. theoretical values of α-WB$_2$, α-AlB$_2$ (P6/mmm) and ω-WB$_2$ (P6$_3$/mmc)structures.
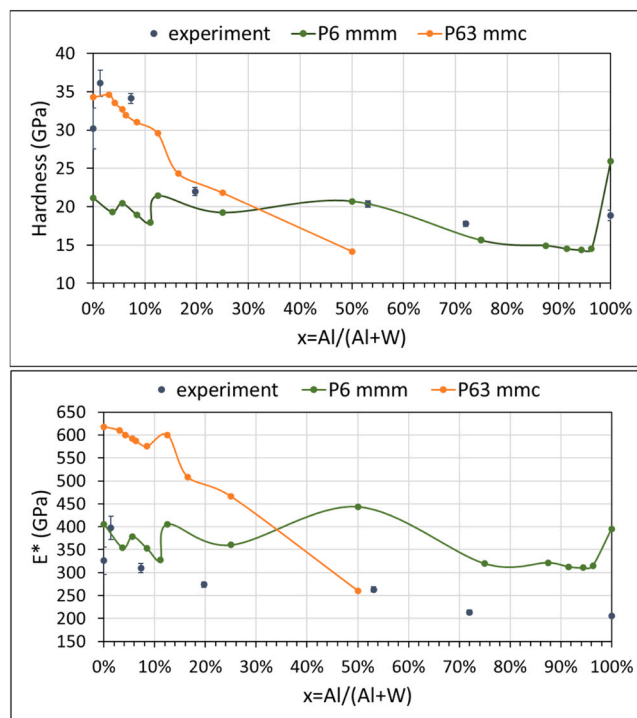

Fig. 7. Hardness and reduced Young's modulus of deposited films vs. theoretical values of α-WB$_2$, α-AlB$_2$ (P6/mmm) and ω-WB$_2$ (P6$_3$/mmc)structures as a function of aluminium content x.

the ω-WB$_2$ P6$_3$/mmc structure is significantly harder (34.27 GPa) than the α-WB$_2$ P6/mmm. This difference results from the arrangement of atoms of both polymorphs and the associated number of covalent and ionic bonds. The addition of aluminium, at a concentration of 3.1 %, results in a slight increase in hardness to 34.63 GPa, associated with solid-solution hardening. A further increase in the amount of aluminium in this structure causes a sharp decrease in both the hardness and Young's modulus. The appearance of aluminium in the crystal lattice of WB$_2$ results in a decrease in the number of strong covalent bonds in favour of less strong ionic bonds. Finally, for x = 50 % aluminium, the hardness drops below 15 GPa. For the metastable α-WB$_2$ P6/mmm structure, the hardness remains approximately 20 GPa up to an aluminium content of 50 %. Then it drops, but for the undoped α-AlB$_2$ P6/mmm structure, it increases to 25.96 GPa. It is due to the lack of tungsten, the boride of which prefers the P6$_3$/mmc structure, which disturbs the P6/mmm crystal lattice of AlB$_2$. For aluminium content x < 30 %, the reduced Young's modulus (Fig. 7) has a value of approximately 350 GPa, which then increases to 443.5 GPa for x = 50 %, and this value is the maximum for this structure.

In the case of experimentally measured hardness, the maximum value reaches 36.1 ± 1.7 GPa for the aluminium content x = 1.4 % (sample #1). This hardness is close to the theoretical values for the P6$_3$/mmc structure. However, XRD studies (Fig. 3) and literature data [6] indicate that, in the case of magnetron deposition, the α-WB$_2$ defective structure should be considered. As shown during the TEM analysis of the microstructure (Fig. 3), the films with the addition of x = 1.4 % and x = 7.3 % of aluminium (samples #2 and #3) have a columnar crystalline structure. Considering the excess of boron, it can form a hard casing on the WB$_2$ columns [68]. Boron atoms are connected by rigid covalent bonds, which increases the strength of the entire system. The literature review indicates that for WB$_2$ doped with titanium, zirconium, or tantalum, the hardness increases due to the formation of vacancies [8, 12]. Theoretical simulations of the WB$_2$ structure with vacancies, carried out in this work, also show an increase in hardness, but it is insignificant (H = 21.89 GPa for α-W$_{0.857}$Al$_{0.143}$B$_2$). In the case of the α-AlB$_2$

structure, the introduction of a vacancy in the form of an AlB_2 particle causes a decrease in hardness to H= 12.78 GPa for α-$W_{0.143}Al_{0.857}B_2$. Another factor contributing to a high hardness value is the measurement of its hardness in the direction perpendicular to the substrate. This is also the direction of column growth, which compresses them. As shown by hardness tests in other directions, their values are much lower [33]. Higher aluminium contents cause the films to be amorphous, which causes a significant decrease in both hardness and Young's modulus. As can be easily observed, the experimental values of the reduced Young's modulus are much lower than the theoretical ones. Replacing tungsten atoms with aluminium atoms of larger atomic radius causes angular distortion and elongation of the B-B covalent bonds. As a result of weakening the covalent bond, elastic softening occurs, and the boride becomes more compressible. As a result, a higher reduction in bulk and Young's moduli occurs [69]. Reduction of the Young's modulus while maintaining high hardness of the crystalline sample #3 results in a relatively high plasticity index $H/E^* > 0.1$ [48].

The analysis of the calculations carried out in the direction of ductility shows significant differences depending on the considered crystal structure. Considering the two classical semi-empirical criteria after Pettifor [70] and Pugh [47], the ductile/brittle material behaviour can be determined. According to them, materials with a positive Cauchy pressure (C_{12}-$C_{44} > 0$) and B/G > 1.75 are ductile, respectively (Fig. 8). In the case of the ω-WB_2 structure, both criteria (Fig. 7) indicate the brittle nature of this structure. The α-WB_2 P6/mmm structure shows a different character. In this case, for all aluminium contents C_{12}-$C_{44} > 17$ GPa and for x < 50 % B/G > 2, which in theory indicates the ductile character of this structure. For the AlB_2 structure, the Cauchy pressure (C_{12}-C_{44}) is greater than 0, but B/G is less than 1.75, which means that this structure possesses a transitional brittle-ductile character.

To determine the response of the films to cracking, an indentation test using a sharp cube corner was conducted [55]. Fig. 9 shows the indentation imprints images obtained during indentation with a load of 150 mN. In all cases, cracks can be observed originating from the corners of the imprint. The shortest cracks were formed for sample #1 without the addition of aluminium. Increasing the amount of aluminium causes the cracks to lengthen, resulting in a decrease in the fracture toughness, K_{IC}. In the case of samples #2 and #3, arc-shaped cracks in the film can be observed along the edges of the indentation, however their nature changes. In the case of sample #3, there are multiple cracks, whereas in sample #2, uniform, large flakes break off. This type of cracking is characteristic of brittle samples.

The nanoindentation toughness values K_{IC}, based on crack lengths and obtained from DFT calculation, are presented in Fig. 10. The addition of Al results in a decrease of experimentally and theoretically

designated values of K_{IC}. The highest determined value of $K_{IC} = 3.8 \pm 0.1$ MPa$\sqrt{m}$ is characteristic of sample 1. This results from its chemical composition, which is closest to the stoichiometric ratio. In the case of samples with the addition of aluminium, the amount of boron increases (Table 4), which causes an additional increase in the brittleness of the films. In the case of samples #2 and #3, the K_{IC} values are close to 3 MPa$\sqrt{m}$ and then decrease to values close to 1 MPa$\sqrt{m}$. It is related to changes in the microstructure of the layers. In the case of samples x > 7.3 %, the microstructure changes from columnar crystalline to amorphous. The change of the ordered structure to amorphous promotes crack propagation and, consequently, a decrease in fracture toughness. As the calculations show, a greater decrease in K_{IC} is observed for the P6$_3$/mmc structure. In this case, the addition of aluminium and its borides, which form in the P6/mmm structure, introduces disturbances in the crystal lattice, and consequently, a decrease in fracture toughness. In the case of the α-WB_2 polymorph, both crystal lattices have the same crystal structure, which results in a much smaller decrease in this parameter. For the undoped α-WB_2 structure, *the K_{IC} is 4.28 MPa$\sqrt{\cdot\,m}$, while for AlB_2 it is 2.64 MPa$\sqrt{\cdot\,m}$. However, the introduction of even 3 % tungsten to this crystal lattice results in a decrease in K_{IC} to the lowest theoretically determined value of $K_{IC} = 2.22$ MPa$\sqrt{m}$.*

4. Conclusions

The paper presents a comparison of mechanical properties, density and thermal conductivity determined using DFT methods with experimentally verified real properties of thin films. The analysis was performed on $W_{1-x}Al_xB_{2+y}$ layers (where x = 0–1). Two WB_2 structures were analyzed theoretically, namely α-WB_2 (P6/mmm) and ω-WB_2 (P6$_3$/mmc) as well as α-AlB_2 (P6/mmm). The layers were deposited with different aluminium contents using a combination of PVD methods, including HiPIMS and DC magnetron sputtering. Due to the higher energy of the pulsed plasma, the films were deposited at 400 °C, in line with earlier results for W-Al-B layers deposited by the DC magnetron sputtering method at higher temperatures. The observations and conclusions resulting from the analysis are as follows:

1. It has repeatedly been shown that using the HiPIMS deposition method, significant densification of the layers can be achieved. The density measurements presented in this work show that the $W_{1-x}Al_xB_{2+y}$ films have a density lower than the theoretical value, attributed to the excess of boron in the deposited layers. This difference decreases as the amount of aluminium increases. A comparison of the P6/mmm and P6$_3$/mmc W-Al-B structures shows lower values of density for the ω-WB_2 structure, while AlB_2 is not stable for this crystal structure.

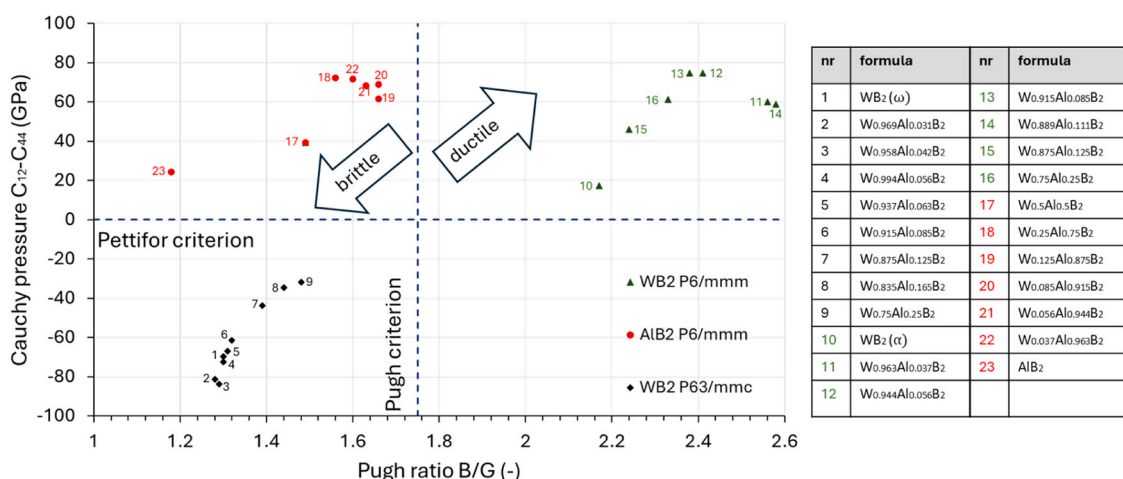| nr	formula	nr	formula
1	WB_2 (ω)	13	$W_{0.915}Al_{0.085}B_2$
2	$W_{0.969}Al_{0.031}B_2$	14	$W_{0.889}Al_{0.111}B_2$
3	$W_{0.958}Al_{0.042}B_2$	15	$W_{0.875}Al_{0.125}B_2$
4	$W_{0.994}Al_{0.056}B_2$	16	$W_{0.75}Al_{0.25}B_2$
5	$W_{0.937}Al_{0.063}B_2$	17	$W_{0.5}Al_{0.5}B_2$
6	$W_{0.915}Al_{0.085}B_2$	18	$W_{0.25}Al_{0.75}B_2$
7	$W_{0.875}Al_{0.125}B_2$	19	$W_{0.125}Al_{0.875}B_2$
8	$W_{0.835}Al_{0.165}B_2$	20	$W_{0.085}Al_{0.915}B_2$
9	$W_{0.75}Al_{0.25}B_2$	21	$W_{0.056}Al_{0.944}B_2$
10	WB_2 (α)	22	$W_{0.037}Al_{0.963}B_2$
11	$W_{0.963}Al_{0.037}B_2$	23	AlB_2
12	$W_{0.944}Al_{0.056}B_2$		

Fig. 8. Plot of DFT-calculated Cauchy pressure (C_{12}-C_{44}) vs. Pugh's ratio (B/G) data, commonly used empirical criteria for ductile/brittle material behaviour.
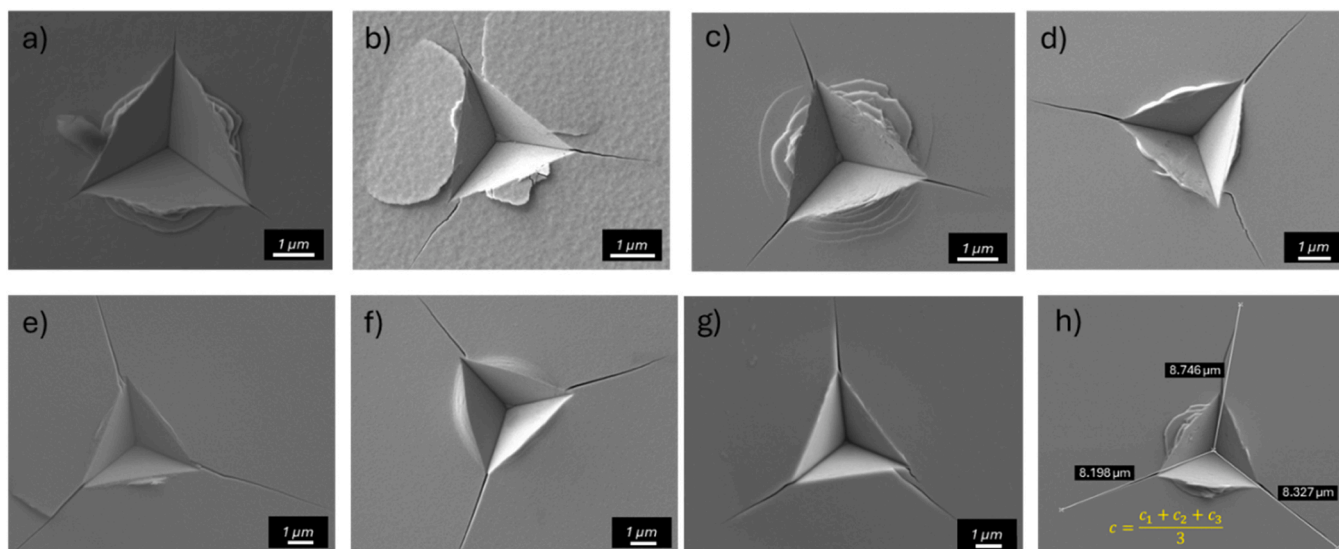
Fig. 9. SEM images of indentation imprints (cube corner indenter) of W-Al-B layers deposited with different aluminium content x (a) 0 %; (b) 1.4 %; (c) 7.3 %; (d) 19.7 %; (e) 53.1 %; (f) 72 %; (g) 100 %; and (h) method of determining the average crack length c.
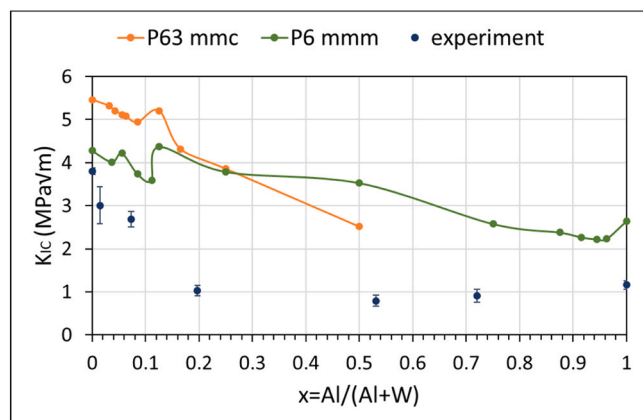

Fig. 10. Fracture toughness of deposited films vs. theoretical values of α-WB$_2$, α-AlB$_2$ (P6/mmm) and ω-WB$_2$ (P6$_3$/mmc)structures as a function of aluminium amount x.

2. In the case of deposition of undoped films using the HiPIMS-DCMS method at 400 °C, an amorphous microstructure is observed. Even a small addition of aluminium (x = 1.4 %) changes the layer growth nature to columnar and results in its crystalline character. Increasing the aluminium content above x = 7.3 % triggers a transformation back to the amorphous state. Such an effect significantly impacts on the decrease of both mechanical properties and thermal conductivity.

3. The obtained films are hard (e.g. H = 36.1 ± 1.7 GPa for x = 1.4 %), but they are characterized by a much lower Young's modulus compared to the results determined theoretically. The relatively high H/E* ratio (> 0.1) for layers with low aluminium content indicates their greater ductility.

4. Ab-initio calculations show that, based on the criteria of Cauchy pressure (C$_{12}$-C$_{44}$) and Pugh's ratio (B/G), the α-WB$_2$ structure may be ductile, in contrast to the other structures. The deposited films are rather brittle in nature, resulting from an excess of boron. The fracture toughness measurements show higher K$_{IC}$ values for lower aluminium content, i.e. 3.8 MPa$\sqrt{\text{m}}$ for undoped WB$_2$, 2.8 MPa$\sqrt{\text{m}}$ for x = 1.4 % and 3 MPa$\sqrt{\text{m}}$ for x = 7.3 % Al, respectively.

5. The experimentally determined thermal conductivity values are in good agreement with the theoretical values. It is important because the values reported in the literature for bulk materials were 10 times higher than the theoretical ones. In the case of boride films, there is no such reference so far. In the case of calculations, these values are lower than the experimental ones (e.g., 1.8 W/mK for α-W$_{0.75}$Al$_{0.25}$B$_2$ vs. 3.3 W/mK for sample #4 x = 19.7 %). This discrepancy may result from an excess amount of boron in the layers, which is a better conductor than WB$_2$.

Analysis of the structure and properties of thin films enables us to understand how different deposition processes affect crystallinity, texture, and other microstructural features, which directly impact the material's mechanical and thermal properties. The appropriate selection of deposition conditions and dopant amount for already known materials allowed us to produce a modern material (layer) such as W$_{1-x}$Al$_x$B$_{2+z}$, which can be applied in industry. Additionally, the theoretical results obtained will allow us to supplement the database necessary for multiscale modelling of both layers and materials in bulk form, where the aluminium alloyed ω-WB$_2$ or α-WB$_2$ structures will be used as the studied materials.

CRediT authorship contribution statement

Tomasz Mościcki: Writing – review & editing, Writing – original draft, Funding acquisition, Data curation, Conceptualization. **Oksana Haponova:** Writing – review & editing. **Jarosław Jasiński:** Writing – review & editing. **Marcin Chmielewski:** Writing – review & editing, Investigation. **Mateusz Włoczewski:** Investigation. **Anna Kosińska:** Investigation. **Katarzyna Zielińska:** Investigation. **Ewa Wojtiuk:** Writing – review & editing, Writing – original draft, Methodology, Investigation, Formal analysis, Conceptualization. **Marcin Maździarz:** Investigation, Formal analysis, Data curation. **Tomasz Stasiak:** Investigation. **Marcin Brykała:** Investigation.

Declaration of Competing Interest

The authors declare the following financial interests/personal relationships which may be considered as potential competing interests: Tomasz reports financial support was provided by National Science Centre. If there are other authors, they declare that they have no known competing financial interests or personal relationships that could have

appeared to influence the work reported in this paper.

Acknowledgements

Appendix A. Supporting information

Supplementary data associated with this article can be found in the online version at doi:10.1016/j.jallcom.2025.185222.

References

[1] A.A. Onoprienko, V.I. Ivashchenko, V.I. Shevche, Structure and properties of the films based on ternary transition metal borides: theory and experiment, Condens. Matter Phys. 26 (2) (2023) 22701, https://doi.org/10.5488/CMP.26.22701.

[2] A. Kvashnin, H. Zakaryan, C. Zhao, Y. Duan, Y. Kvashnina, C. Xie, H. Dong, A. R. Oganov, New tungsten borides, their stability and outstanding mechanical properties, J. Phys. Chem. Lett. 9 (12) (2018) 3470–3477, https://doi.org/10.1021/acs.jpclett.8b01262.

[3] B. Wicher, V. Rogoz, J. Lu, K. Kulikowski, A. Lachowski, S. Kolozsvári, P. Polcik, G. Greczyński, The crucial influence of Al on the high-temperature oxidation resistance of Ti1-xAlxBy diboride thin films (0.36 ≤ x ≤ 0.74, 1.83 ≤ y ≤ 2.03), Appl. Surf. Sci. 686 (2024) 162081, https://doi.org/10.1016/j.apsusc.2024.162081.

[4] C. Gutschka, L. Zauner, T. Glechner, D. Holec, H. Riedl, Metastable AlB2 structured TM-Si-B2±z (TM = Ti, Zr, Hf) solid solutions from first-principles, Acta Mater. 289 (2025) 120857, https://doi.org/10.1016/j.actamat.2025.120857.

[5] M. Vidiš, T. Fiantok, M. Truchly, V. Izai, T. Roch, L. Satrapinskyy, R. Hahn, H. Riedl, P. Švec, V. Šroba, M. Mikula, Enhanced hardness and fracture toughness in diboride superlattice films: Ab initio and experimental study, Surf. Coat. Technol. 515 (2025) 132607, https://doi.org/10.1016/j.surfcoat.2025.132607.

[6] S. Lin, D. Holec, D. Sangiovanni, T. Leiner, L. Hultman, P. Mayrhofer, N. Koutná, Shear-activated phase transformations of diborides via machine-learning potential molecular dynamics, Acta Mater. 301 (2025) 121606, https://doi.org/10.21203/rs.3.rs-5327540/v1.

[7] S. Lin, Z. Chen, R. Janknecht, Z. Zhang, L. Hultman, P. Mayrhofer, N. Koutná, D. Sangiovanni, Machine-learning potentials predict orientation- and mode-dependent fracture in refractory diborides, Acta Mater. 301 (2025) 121568, https://doi.org/10.1016/j.actamat.2025.121568.

[8] C. Fuger, V. Moraes, R. Hahn, H. Bolvardi, P. Polcik, H. Riedl, P. Mayrhofer, Influence of Tantalum on phase stability and mechanical properties of WB2, MRS Commun. 9 (1) (2019) 375–380, https://doi.org/10.1557/mrc.2019.5.

[9] T. Mościcki, R. Psiuk, D. Jarząbek, M. Ciemiorek-Bartkowska, K. Kulikowski, J. Jasiński, M. Włoczewski, M. Lewandowska, Effect of titanium and deposition parameters on microstructure and mechanical properties of W-Ti-B thin films deposited by High Power Impulse Magnetron Sputtering, Surf. Coat. Technol. 485 (2024) 130915, https://doi.org/10.1016/j.surfcoat.2024.130915.

[10] A. Pallas, K. Larsson, Structure determination of the 4d metal diborides: a quantum mechanical study, J. Phys. Chem. B 110 (11) (2006) 5367–5371, https://doi.org/10.1021/jp056652x.

[11] V. Moraes, H. Riedl, C. Fuger, P. Polcik, H. Bolvardi, D. Holec, P.H. Mayrhofer, Ab initio inspired design of ternary boride thin films, 9288, Sci. Rep. 8 (2018) 9288, https://doi.org/10.1038/s41598-018-27426-w.

[12] M. Maździarz, R. Psiuk, A. Krawczyńska, M. Lewandowska, T. Mościcki, Effect of zirconium doping on the mechanical properties of W1−xZrxB2 on the basis of first-principles calculations and magnetron sputtered films, Arch. Civ. Mech. Eng. 22 (193) (2022) 1–30, https://doi.org/10.1007/s43452-022-00513-6.

[13] E. Zhao, J. Meng, Y. Ma, Z. Wu, Phase stability and mechanical properties of tungsten borides from first principles calculations, Phys. Chem. Chem. Phys. 12 (2010) 13158–13165, https://doi.org/10.1039/C004122J.

[14] L. Pangilinan, C. Turner, G. Akopov, M. Anderson, R. Mohammadi, R. Kaner, Superhard tungsten diboride-based solid solutions, Inorg. Chem. 57 (24) (2018) 15305–15313, https://doi.org/10.1021/acs.inorgchem.8b02620.

[15] K. Viskupova, V. Sroba, J. Lu, D. Primetzhofer, B. Wicher, V. Rogoz, T. Roch, M. Truchlý, M. Mikula, I. Petrov, L. Hultman, G. Greczynski, W-ion irradiation promotes TiBx film growth during magnetron sputtering without substrate heating, Surf. Coat. Technol. 497 (2025) 131766, https://doi.org/10.1016/j.surfcoat.2025.131766.

[16] B. Wicher, O. Pshyk, X. Li, B. Bakhit, V. Rogoz, I. Petrov, L. Hultman, G. Greczynski, Superhard oxidation-resistant Ti1-xAlxBy thin films grown by hybrid HiPIMS/DCMS co-sputtering diboride targets without external substrate heating, Mat. Des. 238 (2024) 112727, https://doi.org/10.1016/j.matdes.2024.112727.

[17] C. Hu, S. Lin, M. Podsednik, S. Mráz, T. Wojcik, A. Limbeck, N. Koutná, P. H. Mayrhofer, Influence of co-sputtering AlB2 to TaB2 on stoichiometry of non-reactively sputtered boride thin films, Mater. Res. Lett. 12 (8) (2024) 561–570, https://doi.org/10.1080/21663831.2024.2357700.

[18] R. Hahn, V. Moraes, A. Limbeck, P. Polcik, P.H. Mayrhofer, Electron-configuration stabilized (W,Al)B2 solid solutions, Acta Mater. 174 (2019) 398–405, https://doi.org/10.1016/j.actamat.2019.05.056.

[19] C. Hu, S. Mráz, P.J. Pöllmann, T. Wojcik, M. Podsednik, B. Hajas, A. Limbeck, N. Koutná, J.M. Schneider, P.H. Mayrhofer, Microstructure, mechanical properties, thermal decomposition and oxidation sequences of crystalline AlB2 thin films, Mater. Des. 250 (2025) 113584, https://doi.org/10.1016/j.matdes.2025.113584.

[20] L. Tseng, J. Chen, K. Hsu, W. Wu, C. Chang, Microstructure and mechanical properties of cr-w-b-n coating deposited by dc reactive magnetron co-sputtering, Adv. Mater. Res. 651 (2013) 430–435, https://doi.org/10.4028/www.scientific.net/AMR.651.430.

[21] V. Šroba, T. Fiantok, M. Truchlý, T. Roch, B. Grančič, K. Viskupová, L. Satrapinskyy, P. Švec Jr., Š. Nagy, V. Izai, P. Kúš, M. Mikula, Structure evolution and mechanical properties of Al-alloyed tantalum diboride films prepared by magnetron sputtering co-deposition, J. Vac. Sci. Technol. A 41 (2023) 023410, https://doi.org/10.1116/6.0002390.

[22] M. Alishahi, S. Mirzaei, P. Souček, L. Zábranský, V. Buršíková, M. Stupavská, V. Peřina, K. Balázsi, Z. Czigány, P. Vašina, Evolution of structure and mechanical properties of hard yet fracture resistant w-b-c coatings with varying c/w ratio, Surf. Coat. Technol. 340 (2018) 103–111, https://doi.org/10.1016/j.surfcoat.2018.02.054.

[23] P. Widomski, M. Kaszuba, A. Barełkowski, J. Smolik, D. Garbiec, M. Ciemiorek-Bartkowska, K. Kulikowski, M. Lewandowska, T. Mościcki, Z. Gronostajski, WTaB coatings as effective solutions for increasing die durability in lead-free brass alloy flashless hot forging process, Wear (2025) 205849, https://doi.org/10.1007/s43452-024-01050-0.

[24] J. Radziejewska, R. Psiuk, T. Mościcki, Characterization and wear response of magnetron sputtered w–b and w–ti–b coatings on wc–co tools, Coatings 10 (12) (2020) 1231, https://doi.org/10.3390/coatings10121231.

[25] H. Euchner, P. Mayrhofer, Designing thin film materials — Ternary borides from first principles, Thin Solid Films 583 (2015) 46–49, https://doi.org/10.1016/j.tsf.2015.03.035.

[26] R. Psiuk, J. Chrzanowska-Giżyńska, P. Denis, E. Wyszkowska, M. Wiśniewska, M. Lipińska, E. Wojtiuk, Ł. Kurpaska, J. Smolik, T. Mościcki, Microstructural and properties investigations of tantalum-doped tungsten diboride ceramic coatings via HiPIMS and RF magnetron sputtering, Arch. Civ. Mech. Eng. 24 (2024) 239, https://doi.org/10.1007/s43452-024-01050-0.

[27] C. Yuan, W.M. Waller, M. Kuball, Nanosecond transient thermoreflectance method for characterizing anisotropic thermal conductivity, Rev. Sci. Instrum. 90 (11) (2019) 114903, https://doi.org/10.1063/1.5099961.

[28] X.J. Wang, T. Mori, I. Kuzmych-Ianchuk, Y. Michiue, K. Yubuta, T. Shishido, Y. Grin, S. Okada, D.G. Cahill, Thermal conductivity of layered borides: the effect of building defects on the thermal conductivity of TmAlB4 and the anisotropic thermal conductivity of AlB2, APL Mater. 2 (2014) 046113, https://doi.org/10.1063/1.4871797.

[29] M.S. Kovalchenko, L.G. Bodrova, V.F. Nemchenko, V.F. Kolotun, Some physical properties of the higher borides of molybdenum and tungsten, J. Less Common Met. 67 (2) (1979) 357–362, https://doi.org/10.1016/0022-5088(79)90012-2.

[30] P. Li, L. Ma, M. Peng, B. Shu, Y. Duan, Elastic anisotropies and thermal conductivities of WB2 diborides in different crystal structures: a first-principles calculation, J. Alloy. Compd. 747 (2018) 905–915, https://doi.org/10.1016/j.jallcom.2018.03.109.

[31] X. Gu, C. Liu, H. Guo, K. Zhang, C. Chen, Sorting transition-metal diborides: new descriptor for mechanical properties, Acta Mater. 207 (2021) 116685, https://doi.org/10.1016/j.actamat.2021.116685.

[32] Z. Chen, Y. Huang, N. Koutná, Z. Gao, D. Sangiovanni, S. Fellner, G. Haberfehlner, S. Jin, P. Mayrhofer, G. Kothleitner, Z. Zhang, Large mechanical properties enhancement in ceramics through vacancy-mediated unit cell disturbance, Nat. Commun. 14 (2023) 8387, https://doi.org/10.1038/s41467-023-44060-x.

[33] C. Fuger, R. Hahn, L. Zauner, T. Wojcik, M. Weiss, A. Limbeck, O. Hunold, P. Polcik, H. Riedl, Anisotropic super-hardness of hexagonal WB2±z thin films, Mater. Res. Lett. 10 (2) (2021) 70–77, https://doi.org/10.1080/21663831.2021.2021308.

[34] P. Hohenberg, W. Kohn, Inhomogeneous electron gas, Phys. Rev. 136 (1964) 864–871, https://doi.org/10.1103/PhysRev.136.B864.

[35] W. Kohn, L. Sham, Self-consistent equations including exchange and correlation effects, Phys. Rev. 140 (1965) 1133–1138, https://doi.org/10.1103/PhysRev.140.A1133.

[36] D. Hamann, X. Wu, K.M. Rabe, D. Vanderbilt, Metric tensor formulation of strain in density-functional perturbation theory, Phys. Rev. B 71 (2005) 035117, https://doi.org/10.1103/PhysRevB.71.035117.

[37] X. Gonze, B. Amadon, G. Antonius, F. Arnardi, L. Baguet, J.-M. Beuken, J. Bieder, F. Bottin, J. Bouchet, E. Bousquet, N. Brouwer, F. Bruneval, G. Brunin, T. Cavignac, J.-B. Charraud, W. Chen, M. Cote, S. Cottenier, J. Denier, G. Geneste, P. Ghosez, M. Giantomassi, Y. Gillet, O. Gingras, D. Hamann, G. Hautier, X. He, N. Helbig, N. Holzwarth, Y. Jia, F. Jollet, W. Lafargue-Dit-Hauret, K. Lejaeghere, M.A.L. Marques, A. Martin, C. Martins, H. Miranda, F. Naccarato, K. Persson, G. Petretto, V. Planes, Y. Pouillon, S. Prokhorenko, F. Ricci, G.-M. Rignanese, A. Romero, M. Schmitt, M. Torrent, M. van Setten, B. Troeye, M. Verstraete, G. Zerah, J. Zwanziger, The ABINIT project: impact, environment and recent developments, Comput. Phys. Commun. 248 (2020) 107042, https://doi.org/10.1016/j.cpc.2019.107042.

[38] J. Perdew, Y. Wang, Accurate and simple analytic representation of the electron-gas correlation energy, Phys. Rev. B 45 (1992) 13244–13249, https://doi.org/10.1103/PhysRevB.45.13244.

[39] F. Jollet, M. Torrent, N. Holzwarth, Generation of projector augmented-wave atomic data: A 71 element validated table in the XML format, Comput. Phys. Commun. 185 (4) (2014) 1246–1254, https://doi.org/10.1016/j.cpc.2013.12.023.

[40] C. Qi, Y. Jiang, Y. Liu, R. Zhou, Elastic and electronic properties of XB2 (X=V, Nb, Ta, Cr, Mo, and W) with AlB2 structure from first principles calculations, Ceram. Int. 40 (4) (2014) 5843–5851, https://doi.org/10.1016/j.ceramint.2013.11.026.

[41] M. Mazdziarz, T. Moscicki, Structural, mechanical, optical, thermodynamical and phonon properties of stable ReB2 polymorphs from density functional calculations, J. Alloy. Compd. 657 (2016) 878–888, https://doi.org/10.1016/j.jallcom.2015.10.133.

[42] R. Hill, The elastic behaviour of a crystalline aggregate, Proc. Phys. Soc. Sect. A 65 (5) (1952) 349–354, https://doi.org/10.1088/0370-1298/65/5/307.

[43] M. Maździarz, M. Gajewski, Estimation of isotropic hyperelasticity constitutive models to approximate the atomistic simulation data for aluminium and tungsten monocrystals, Comput. Model. Eng. Sci. 105 (2) (2015) 123–150, https://doi.org/10.3970/cmes.2015.105.123.

[44] G. Grimvall, B. Magyari-Kope, V. Ozolins, K.A. Persson, Lattice instabilities in metallic elements, Rev. Mod. Phys. 84 (2012) 945–986, https://doi.org/10.1103/RevModPhys.84.945.

[45] M. Maździarz, Mechanical stability conditions for 3D and 2D crystals under arbitrary load, Arch. Mech. 4 (2025) 379–399, https://doi.org/10.24423/aom.4679.

[46] E. Mazhnik, A. Oganov, Application of machine learning methods for predicting new superhard materials, J. Appl. Phys. 128 (7) (2020) 075102, https://doi.org/10.1063/5.0012055.

[47] S. Pugh, XCII. Relations between the elastic moduli and the plastic properties of polycrystalline pure metals, Lond. Edinb. Dublin Philos. Mag. J. Sci. 45 (367) (1954) 823–843, https://doi.org/10.1080/14786440808520496.

[48] J. Musil, Flexible hard nanocomposite coatings, RSC Adv. 5 (2015) 60482, https://doi.org/10.1039/C5RA09586G.

[49] D. Clarke, Materials selection guidelines for low thermal conductivity thermal barrier coatings, Surf. Coat. Technol. 163-164 (2003) 67–74, https://doi.org/10.1016/S0257-8972(02)00593-5.

[50] D. Cahill, S. Watson, R. Pohl, Lower limit to the thermal conductivity of disordered crystals, Phys. Rev. B 46 (1992) 6131–6140, https://doi.org/10.1103/PhysRevB.46.6131.

[51] R. Psiuk, T. Mościcki, J. Chrzanowska-Giżyńska, Ł. Kurpaska, J. Radziejewska, P. Denis, D. Garbiec, M. Chmielewski, Mechanical and thermal properties of W-Ta-B coatings deposited by high-power impulse magnetron sputtering (HiPIMS), Materials 16 (2) (2023) 664, https://doi.org/10.3390/ma16020664.

[52] T. Mościcki, R. Psiuk, J. Radziejewska, M. Wiśniewska, D. Garbiec, Properties of spark plasma sintered compacts and magnetron sputtered coatings made from Cr, Mo, Re and Zr alloyed tungsten diboride, Coatings 11 (2021) 1378, https://doi.org/10.3390/coatings11111378.

[53] D. Nečas, P. Klapetek, Gwyddion: an open-source software for SPM data analysis, Open Phys. 10 (1) (2012) 181–188, https://doi.org/10.2478/s11534-011-0096-2.

[54] W. Oliver, G. Pharr, Measurement of hardness and elastic modulus by instrumented indentation: advances in understanding and refinements to methodology, J. Mater. Res. 18 (2004) 3–20, https://doi.org/10.1557/jmr.2004.19.1.3.

[55] B. Lawn, A. Evans, D. Marshall, Elastic/plastic indentation damage in ceramics: the median/radial crack system, J. Am. Ceram. Soc. 63 (1980) 574–581, https://doi.org/10.1111/j.1151-2916.1980.tb10768.x.

[56] T. Yagi, K. Ohta, K. Kobayashi, N. Taketoshi, K. Hirose, T. Baba, Thermal diffusivity measurement in a diamond anvil cell using a light pulse thermoreflectance technique, Meas. Sci. Technol. 22 (2) (2011) 024011, https://doi.org/10.1088/0957-0233/22/2/024011.

[57] T. Baba, T. Baba, T. Mori, Fourier transform thermoreflectance method under front-heat front-detect configuration, Int. J. Thermophys. 45 (2024) 61, https://doi.org/10.1007/s10765-024-03351-1.

[58] L. Mitterhuber, E. Kraker, S. Defregger, Structure function analysis of temperature-dependent thermal properties of nm-thin Nb2O5, Energies 12 (4) (2019) 610, https://doi.org/10.3390/en12040610.

[59] A. Blinder, A. Bolgar, Heat capacity and enthalpy of transition-metal borides in a broad range of temperatures 30(12), Sov. Powder Metall. Met. Ceram. (1991) 1053–1056, https://doi.org/10.1007/BF00794439.

[60] X. Zhu, X. Gao, H. Song, G. Han, D.-Y. Lin, Effects of vacancies on the mechanical properties of zirconium: an ab initio investigation, Mater. Des. 119 (2017) 30–37, https://doi.org/10.1016/j.matdes.2017.01.060.

[61] M. Maździarzi, T. Mościcki, New zirconium diboride polymorphs - first-principles calculations, Materials 13 (2020) 3022, https://doi.org/10.3390/ma13133022.

[62] P. Barna, M. Adamik, Fundamental structure forming phenomena of polycrystalline films and the structure zone models, Thin Solid Films 317 (1998) 27–33, https://doi.org/10.1016/S0040-6090(97)00503-8.

[63] D. Williams, C. Carter, Transmission Electron Microscopy; a Textbook for Materials Science, Springer Science + Business Media, New York, NY, 2009, https://doi.org/10.1007/978-0-387-76501-3.

[64] G. Greczynski, I. Petrov, J. Greene, L. Hultman, Paradigm shift in thin-film growth by magnetron sputtering: From gas-ion to metal-ion irradiation of the growing film, J. Vac. Sci. Technol. A 37 (2019) 060801, https://doi.org/10.1116/1.5121226.

[65] F. Wagner, A. Baranov, Y. Grin, M. Kohout, A position-space view on chemical bonding in metal diborides with AlB2 type of crystal structure, Z. Anorg. Allg. Chem. 639 (11) (2013) 2025–2035, https://doi.org/10.1002/zaac.201200523.

[66] A. Yang, Y. Duan, M. Peng, L. Shen, H. Qi, Elastic properties, fracture toughness, ideal tensile strength and thermal conductivities of the stable hexagonal WB2, W2B5, WB3, and WB4, Appl. Phys. A 128 (2022) 152, https://doi.org/10.1007/s00339-022-05299-1.

[67] X. Wang, T. Mori, I. Kuzmych-Ianchuk, Y. Michiue, K. Yubuta, T. Shishido, Y. Grin, S. Okada, D. Cahill, Thermal conductivity of layered borides: the effect of building defects on the thermal conductivity of TmAlB4 and the anisotropic thermal conductivity of AlB2, APL Mater. 2 (2014) 046113, https://doi.org/10.1063/1.4871797.

[68] P.H. Mayrhofer, C. Mitterer, J. Wen, J. Greene, I. Petrov, Self-organized nanocolumnar structure in superhard TiB2 thin films, Appl. Phys. Lett. 86 (2005) 131909, https://doi.org/10.1063/1.1887824.

[69] P. Sharma, G. Balasubramanian, Electronic and lattice distortions induce elastic softening in refractory multicomponent borides, Chem. Mater. 35 (2023) 7511–7520. ⟨https://pubs.acs.org/doi/10.1021/acs.chemmater.3c01086⟩.

[70] D. Pettifor, Theoretical predictions of structure and related properties of intermetallics, Mater. Sci. Technol. 8 (1992) 345–349, https://doi.org/10.1179/mst.1992.8.4.345.